Journal of Extracellular Vesicles

RESEARCH ARTICLE OPEN ACCESS

Inhibitors of Tax1-PDZ Interactions Block HTLV-1 Viral Transmission by Changing EV Composition

Jedidja Puttemans[1] | Yasmine Brammerloo[1] | Karim Blibek[1] | Jeremy Blavier[1] | Thandokuhle Ntombela[1] | Inge Van Molle[2] | Julie Joseph[3] | Julien Olivet[1,4] | Deeya Saha[1,5] | Manon Degey[6] | Malik Hamaidia[7] | Pooja Jain[3] | Piel Geraldine[6] | Pascale Zimmermann[8,9] | Dae-Kyum Kim[10,11,12] | Dominique Baiwir[13] | Makon-Sébastien Njock[14] | Franck Dequiedt[15] | Kourosh Salehi-Ashtiani[16] | Steven Ballet[17] | Alexander N. Volkov[2,18] | Jean-Claude Twizere[1,16,19] | Sibusiso B. Maseko[1]

[1]Laboratory of Viral Interactomes, Unit of Molecular Biology of Diseases, GIGA Institute, University of Liege, Liège, Belgium | [2]VIB-VUB Center for Structural Biology, Flemish Institute of Biotechnology (VIB), Pleinlaan 2, Brussels, Belgium | [3]Department of Microbiology & Immunology, Drexel University College of Medicine, Philadelphia, Pennsylvania, USA | [4]Structural Biology Lab, Molecular Structural & Translational Virology Group, Rega Institute for Medical Research and Department of Microbiology, Immunology and Transplantation, KU Leuven, Leuven, Belgium | [5]Dept. Of Biotechnology, Faculty of Life and Allied Health Sciences (FLAHS), M.S Ramaiah University of Applied Sciences (MSRUAS), Bangalore, India | [6]Laboratoire de Technologie Pharmaceutique & Biopharmacie (LTPB), CIRM, University of Liège, Liège, Belgium | [7]Laboratory of Cellular and Molecular Epigenetics, Cancer Unit, GIGA Institute, University of Liège, Liège, Belgium | [8]Aix Marseille Univ, CNRS, INSERM, Institut Paoli-Calmettes, CRCM, Equipe labellisée Ligue Cell polarity, Cell signaling and Cancer, Marseille, France | [9]Department of Human Genetics, KU Leuven, Leuven, Belgium | [10]Division of Thoracic and Upper Gastrointestinal Surgery, Department of Surgery, Faculty of Medicine and Health Sciences, McGill University, Montreal, Canada | [11]Cancer Research Program, Research Institute of McGill University Health Centre, Montreal, Canada | [12]Montreal General Hospital Foundation, McGill University Health Centre, Montreal, Canada | [13]GIGA proteomics platform, University of Liège, Liège, Belgium | [14]Laboratory of Pneumology, GIGA Institute, University of Liège, Liège, Belgium | [15]Laboratory of Gene Expression and Cancer, Molecular Biology of Diseases Unit, GIGA Institute, University of Liège, Liège, Belgium | [16]Division of Science and Math, New York University Abu Dhabi, Abu Dhabi, UAE | [17]Research Group of Organic Chemistry, Vrije Universiteit Brussel (VUB), Brussels, Belgium | [18]Jean Jeener NMR Centre, Vrije Universiteit Brussel (VUB), Pleinlaan 2, Brussels, Belgium | [19]TERRA research and teaching centre, Microbial Processes and Interactions (MiPI), Gembloux Agro Bio-tech, University of Liège, Gembloux, Belgium

Correspondence: Jean-Claude Twizere (jean-claude.twizere@uliege.be) | Sibusiso B. Maseko (sbmaseko@uliege.be)

Received: 17 December 2024 | **Revised:** 26 May 2025 | **Accepted:** 6 July 2025

Funding: This work was primarily supported by the FWO-FRS-FNRS Weave grant TW01423F to Steven Ballet, Jean-Claude Twizere and Alexander N. Volkov, FRS-FNRS Televie grants 30823819 to Jean-Claude Twizere; Fund for Research Training in Industry and Agriculture grant 24343558 to Karim Blibek. Franck Dequiedt is a Chercheur Qualifié Honoraire, Jean-Claude Twizere a Research Director, Sibusiso B. Maseko is a postdoctoral fellow of the F.R.S.-FNRS. Sibusiso B. Maseko is further supported by the Funds Suzanne Dechesne, Serge Rousseau and Docteur Jean Gerald, Managed by King Boudouin Foundation. Pascale Zimmermann's lab work was funded by La Ligue Nationale Contre le Cancer (Label 2018), the Fund for Scientific Research Flanders (FWO, G0C5718N) and the internal funds of the KU Leuven (C14/20/105). Q Exactive mass spectrometer (GIGA Proteomics Facility) was acquired thanks to EDRF and Walloon Region funding. This research was also supported by NYUAD Faculty Research Funds (AD060) from the Division of Science (NYUAD, UAE) The funders had no role in study design, data collection and analysis, decision to publish, or preparation of the manuscript.

Keywords: interactome | miRNA | PDZ | syntenin-1 | Tax-1

ABSTRACT

Extracellular vesicles (EVs) are known to facilitate infection by enveloped RNA viruses including the Human T-cell leukemia virus type-1 (HTLV-1). HTLV-1-encoded proteins, like the transactivator and oncoprotein Tax-1, are loaded into EVs but their precise impact on EV cargos is not yet known. Here, we report a comprehensive interaction map between Tax-1 and the human

Jedidja Puttemans and Yasmine Brammerloo contributed equally to this work.

PDZ (PSD95/DLG/ZO-1) proteins that regulate EVs formation and composition. We show that Tax-1 interacts with more than one-third of hPDZome components, including proteins involved in cell cycle, cell–cell junctions, cytoskeleton organization and membrane complex assembly. We extensively characterized Tax-1 interaction with syntenin-1, an evolutionary conserved PDZ hub that controls EV biogenesis. Using nuclear magnetic resonance (NMR) spectroscopy, we have determined the structural basis of the interaction between the *C*-terminal PDZ binding motif of Tax-1, and two PDZ domains of syntenin-1. Importantly, we show that a small molecule able to inhibit HTLV-1 cell-to-cell transmission breaks the Tax-1/syntenin-1 interaction, impacts the levels of syntenin-1 and viral proteins in EVs, and shifts the EV composition toward cellular antiviral proteins and microRNAs, including the miR-320 family. Consequently, we demonstrate that mimics of miR-320c, encapsulated into EVs, have antiviral activities with a potential to be used against HTLV-1 induced diseases.

1 | Introduction

Human T-cell lymphotropic virus type 1 (HTLV-1) is a retrovirus infecting T-cells and associated with several diseases, including adult T-cell leukemia/lymphoma (ATL) and HTLV-1-associated myelopathy/tropical spastic paraparesis (HAM/TSP) (Nozuma et al. 2020). HTLV-1 transmission occurs via cell-to-cell contacts while cell-free viruses remain poorly infectious. Extracellular vesicles (EVs) are among the carriers described in the intercellular transmission routes for HTLV-1 (Arone et al. 2023). EVs represent a heterogeneous population of membrane-bound vesicles secreted by most cell types. Based on biogenesis, EVs can be broadly grouped into categories such as exosomes (originating from the endosomal pathway), microvesicles or ectosomes (shed directly from the plasma membrane), and other vesicle-like structures including apoptotic bodies, large oncosomes, and virus-like particles (Théry et al. 2018; Van Niel et al. 2018; Kowal et al. 2014). Exosomes are nanoscale bio-vesicles (30–200 nm) that are released into bodily fluids when the plasma membrane and multivesicular bodies fuse. They have been demonstrated to transport nucleic acids, proteins and lipids that are specific to a given cell. They can also be selectively absorbed by nearby or distant cells, regulating the recipient cells in response to their bioactive substances (Zhang et al. 2019). Protein content of ectosomes and exosomes were experimentally determined in numerous studies and are compiled in the EVpedia web portal (https://evpedia.info/evpedia2_xe/). This proteomic composition drives EV biogenesis, enrichment in biological functions and dictate their roles in viral transmission (Kim et al. 2015). In this context, a class of proteins called PDZ (PSD-95/Discs Large/ZO-1) appears as important targets as they regulate EVs production, composition and uptake (Castro-Cruz et al. 2023) and they interplay with various viral proteins including the HTLV-1 encoded transactivator protein known as Tax-1 (Trans-Activator of X gene). Tax-1 is a multifunctional protein that plays a pivotal role in the HTLV-1 life cycle and pathogenesis. It is primarily implicated in regulating viral gene expression by interacting with transcription factors such as CREB/ATF1, CBP/p300, PCAF, NF-Kb, AP-1 (Kwok et al. 1996; Kfoury et al. 2012; Zhao and Giam 1991; Seiki et al. 1988) and post-transcriptional regulators such as RNA splicing factors A1CF and U2AF2 (Vandermeulen et al. 2021). The interplay of the above factors regulates viral replication, ensuring continued presence of HTLV-1 in the host and facilitating viral persistence (Currer et al. 2012). Additionally, Tax-1 contributes to immune evasion by suppressing host immune responses and promoting viral dissemination (Bangham et al. 2015). Tax-1 interactions with host cell signalling pathways and transcription factors can lead to cellular transformation and the development of ATL. Furthermore, Tax-1 is implicated in the induction of genomic instability and inflammation, which are crucial factors in the pathogenesis of HTLV-1-associated diseases (Matsuoka and Jeang 2011). Being a multi-domain protein, Tax-1 has been shown to interact with more than 200 partners (Vandermeulen et al. 2021; Maseko et al. 2023). Among these are PDZ proteins, which bind to the *C*-terminal of Tax-1. The human genome contains about 256 PDZ domains in 149 proteins, several of which have been reported to interact with Tax-1 (Maseko et al. 2023; Ivarsson et al. 2014; Xie et al. 2006).

PDZ domains mediate specific protein–protein interactions (PPI) by binding to short peptide sequences, called the PDZ binding motif (PBM), typically located at the *C*-terminus of target proteins. These short peptides often conform to a consensus motif, such as (S/T)-X-(V/I/L)-COOH, where X represents any amino acid (Nardella et al. 2021). PDZ proteins are involved in the assembly of multiprotein complexes at specific subcellular locations, such as the plasma membrane or cellular junctions, and contribute to the spatial and temporal organization of cellular signalling pathways. Additionally, PDZ proteins are involved in the regulation of cell polarity and cell–cell junctions, influencing processes like epithelial cell adhesion and migration (Castro-Cruz et al. 2023; Pérès et al. 2018). The Tax-1 PDZ interactions have implications in the HTLV-1 induced leukomogenesis process. It has been shown that Tax-1 PBM promotes transformation of rat fibroblasts and mouse lymphocytes in vitro (Pérès et al. 2018). This is not the case with HTLV-2 lacking the PBM and thereby making the PDZ -Tax-1 a promising therapeutic target.

In this study, we comprehensively mapped the Tax-1 interactome with human PDZ-containing proteins and found that about one-third of the human PDZome is capable of specific interactions with Tax-1. Using nuclear magnetic resonance (NMR) spectroscopy, we structurally characterized interactions between Tax-1 PBM and PDZ domains of syntenin-1, also known as syndecan binding protein (SDCBP) which is the most connected PDZ containing protein in the cytoskeleton. We hypothesized that a small molecule binding to syntenin-1 PDZ domains will also inhibit HTLV-1 cell-to-cell transmission. We further extensively characterized EVs from HTLV-1 producing cells treated with a small molecule able to inhibit Tax-1/syntenin-1 interaction and demonstrated that this inhibition is associated with recruit-

ment of specific microRNAs into EVs and viral transmission impairment.

2 | Material and Methods

Predicting potential Tax-1 interactors using in silico motif-domain and domain-domain based strategies. This is described in detail in the Supporting Information.

2.1 | Cell Culture

HEK293T and HeLa cell lines were cultured in DMEM (Dulbecco's Modified Eagle's Medium) containing 10% FBS (Foetal Bovine Serum), 2 mM glutamine, and antibiotics (Penicillin 100U/mL, Streptomycin 100U/mL). Lymphocyte cell lines (Jurkat, Jurkat-LTR-Luc, JPX9, CEM, CTV1, MOLT16, HuT 78) were maintained in culture in RPMI medium (Roswell Park Memorial Institute medium), 2 mM glutamine, and antibiotics (Penicillin 100U/mL, Streptomycin 100 µg/mL). Lymphocyte cell lines infected with HTLV-1 (MT2, MT4, HuT 102, C8145, C91PL) were cultured under the same conditions as lymphocyte cell lines not infected with HTLV-1, with addition of biosafety level L2 containment measures. All cells were incubated at 37°C with 5% CO_2.

2.2 | Transient Transfections

HEK293T or lymphocyte cells cultured to 80% confluency were transfected using polyethyleneimine (PEI). The medium was changed before transfection, and cells were collected 24 h after transfection. The culture medium was changed 24 h post transfection and cells were harvested 48 h post transfection.

2.3 | Yeast Two-Hybrid Interactome Mapping of Tax-1 With Individual Human PDZ Domains

The Gateway cloning method was used to transfer DNA encoding the PDZ domain into the AD yeast expression vector pACT2. All PDZ domains were transformed into the yeast haploid strain Y187 (MATa, ura3-52, his3-200, ade2-101, leu2-3, 112, gal4Δ, met-, gal80Δ, MEL1, URA3: GAL1UAS -GAL1TATA -lacZ). Similarly, the DNA fragment encoding Tax-1 was cloned into the DB yeast expression vector pGBT9 and transformed next into the haploid yeast strain AH109 (MATa, trp1-901, leu2-3, 112, Ura3 -52, his3-200, gal4Δ, gal80Δ, LYS2: GAL1UAS-GAL1TATA-HIS3, GAL2UASGAL2TATA-ADE2, URA3: MEL1UAS-MEL1TATA-lacZ, MEL1). The interactions between each PDZ and Tax-1 were tested by conjugation of the two strains of yeast. Briefly, overnight co-culture of the two types of yeast (of the opposite mating type) was performed. Growth of diploid cells was done by growing them in a selective medium favouring diploid yeast (liquid yeast extract Peptone-Dextrose YPAD –W Tryptophan –L Leucine) supplemented with 10% PEG for 4 h at 30°C and via gentle stirring. After washing with water, the yeasts were placed on a solid Tryptophan-Histidine-Leucine (-WHL) selective medium for phenotypic assay. Diploid yeasts which proliferate on the -WHL medium indicate an interaction between the two fusion proteins.

2.4 | Gaussia Princeps Luciferase Complementation Assay (GPCA)

HEK293T cells were seeded in 24-well plates and transfected with GL1 and/or GL2 plasmids expressing the fusion proteins 24 h later. Luciferase activity was measured on the lysates in 96-well plates. The normalized luciferase ratio was calculated as follows: NLR = co-transfection luciferase value (GL1 + GL2)/(GL1 luciferase value alone + GL2 luciferase value alone). An interaction was considered positive or validated when NLR ≥ 3.5, as previously determined (Muller et al. 2013; Neveu et al. 2012). Cell lysis and luminescence measurements were performed in triplicate for each condition.

2.5 | Measurement of Luciferase Activity

Collected cells were lysed with the passive lysis buffer (Promega). For luciferase measurements, 100 µL of the lysates were used, to which the substrates for Firefly and Renilla luciferases 'stop & glo' (Promega) were added. Luciferase measurements were performed in 96-well plates using an automated DLR machine. Firefly luciferase values were normalized to Renilla luciferase values, and the calculated ratio represents luciferase activity.

2.6 | GST Pulldown

To detect Tax-1 partners by pulldown, PDZ domains fused to a Flag tag were expressed in HEK293T cells. GST-Tax-1, or GST-Tax-2 protein as negative control, were expressed separately and then purified with Glutathione Sepharose beads. Beads containing the fusion proteins were then incubated with PDZ-Flag containing cell lysates and washed. The detection of Flag by immunoblot was indicative of an interaction between Tax-1 and the PDZ domain protein.

2.7 | Immunoblots

The cells or EVs were lysed using IPLS (Immunoprecipitation Low Salt; Tris-HCl pH 7.5 50 mM, EDTA, pH 8, 0.5 mM, 0.5% NP-40, 10% glycerol, 120 mM NaCl, complete Protease Inhibitor (Roche)) and clarified by centrifugation. After incubating the lysate for 5 min at 100°C in the presence of Laemmli buffer, electrophoresis was carried out on 10% SDS-PAGE, followed by immunoblotting. The following antibodies were used: anti-Flag, anti-syntenin-1, anti-Tax-1, anti-ubiquitin, anti-calnexin, anti-Alix, anti HSP70.

2.8 | Synthetic Peptide

The Tax-1 10-mer (H-SEKHFRETEV-OH), 4-mer (ETEV) and 6-mer (SEKHFR) peptides were synthesized by Biomatik, Canada, as acetate salts of >98% purity.

2.9 | Expression and Purification

PDZ domains of syntenin-1 (PDZ1, PDZ2 and tandem PDZ1+PDZ2) were synthesized by GeneScript and cloned into pGEX-6P-1. Protein expression was done in *Escherichia coli* BL21 as previously reported (Maseko et al. 2023). Briefly, a single bacterial colony was used to inoculate 5.0 mL LB and grown overnight at 37°C, from which 1.0 mL was used as a starter culture for expressing the proteins in 100 mL LB. For expression, the culture was grown at 37°C, shaking (180 rpm) until $OD6_{00}$ reached 0.4–0.6, then induced by the addition of 1.0 mM IPTG and further grown for 4 h under the same conditions. The isotopically labelled U [^{13}C,^{15}N] or U- [^{15}N] proteins were produced in *E. coli* grown in the minimal medium following a published protocol (Volkov and van Nuland 2013). GST-fused proteins were purified using glutathione Sepharose 4B beads (GE HealthCare) equilibrated in 1× Phosphate Buffered Saline (PBS) buffer. GST-tagged PDZ domains were eluted with 50 mM Tris, pH 8, 10 mM reduced glutathione. GST tag was then cleaved off using preScission protease (Sigma) overnight at 4°C. The mixture was then loaded back to the column equilibrated in PBS, and PDZ proteins were collected from the flow-through. These were further purified using a HiPrep 16/60 Sephacryl S-100 HR size exclusion column, equilibrated in 20 mM NaPi pH 6.0, 50 mM NaCl, 2 mM DTT.

2.10 | NMR Spectroscopy

All NMR spectra were acquired at 298 K in 20 mM sodium phosphate 50 mM NaCl pH 6.0, 2 mM DTT and 10 % D_2O for the lock on a Bruker Avance III HD 800 MHz spectrometer (equipped with a TCI cryoprobe) or a Varian Direct-Drive 600 MHz spectrometer (fitted with a PFG-Z cold probe). The data were processed in NMRPipe (Delaglio et al. 1995) and analysed in CCPNMR (Vranken et al. 2005). The assignments of backbone resonances of the individual syntenin-1 PDZ1 and PDZ2 domains were obtained from 0.7 to 1.1 mM U- [^{13}C,^{15}N] protein samples using a standard set of 3D BEST HNCACB, HN(CO)CACB, HNCO and HN(CA)CO experiments and aided by the published assignments (Cierpicki et al. 2005; Grembecka et al. 2006). Subsequently, the NMR assignments of the individual PDZ domains were transferred to the spectrum of syntenin-1 PDZ1+2 tandem and verified by standard triple-resonance experiments. The chemical shift perturbation experiments and NMR titrations were performed by incremental addition of 10 mM stock solutions of Tax peptide to U- [^{15}N] or U- [^{13}C,^{15}N] protein samples at the initial concentration of 0.3 mM. At each increment, changes in chemical shifts of the protein resonances were monitored in 2D [^{1}H,^{15}N] HSQC spectra. The average amide chemical shift perturbations ($\Delta\delta_{avg}$) were calculated as $\Delta\delta_{avg} = (\Delta\delta_N{}^2/50+\Delta\delta_H{}^2/2)^{0.5}$, where $\Delta\delta_N$ and $\Delta\delta_H$ are the chemical shift perturbations of the amide nitrogen and proton, respectively. The NMR titration curves were analysed with a two-parameter nonlinear least squares fit using a one-site binding model corrected for the dilution effect (Kannt et al. 1996), Equation (1):

$$\Delta\delta_{binding} = 0.5\Delta\delta_0\left(A - \sqrt{A^2 - 4R}\right)$$

$$A = 1 + R + K_D\frac{[peptide]_0 + R[protein]_0}{[peptide]_0[protein]_0}, \quad (1)$$

where $\Delta\delta$binding is the chemical shift perturbation at a given protein/peptide ratio; $\Delta\delta 0$ is the chemical shift perturbation at 100 % peptide bound; R is the [peptide]/[protein] ratio at a given point; [protein]0 and [peptide]0 are the concentrations of the starting protein sample and the peptide titrant stock solution, respectively; and KD is the equilibrium dissociation constant.

2.11 | Fluorescence Polarization (FP)

GST tagged syntenin-1_PDZ1+2 was used in fluorescence polarization competition experiments. Firstly, we wanted to find a concentration that gives enough FP signal, note that the interaction between Tax and syntenin-1 is weak. In the competition experiment, 50 μM of protein, 25 nM of FITC-SEKHFRETEV (Tax-1-10mer) and small molecule concentration of 0–1000 μM was used. To study the inhibition, the small molecules syntOFF (Leblanc et al. 2020) and iTax/PDZ-01 (Maseko et al. 2023) were incubated with the protein in a final volume of 10 μL in 384 well Corning black plates (cat# 3544) and incubated for 2 h at room temperature. This was followed by the addition of 25 nM of fluorescently labelled peptide and further incubated for 1 h. Fluorescence polarization was then read out in a Flex station 3, Molecular Devices (excitation 485 nm and emission at 520 nm).

2.12 | Purification of EVs

HuT 102 or Jurkat cells (3.0×10^6 cells) were cultured in 10 mL RPMI supplemented with 10% exosome depleted FBS (Ref A2720803) from Thermo Scientific. The cells were treated with 25 μM of iTax/PDZ-01 or DMSO to a final concentration of 0.13 % as a vehicle control in triplicates for 96 h. EVs were isolated from cell supernatants using the total exosome isolation reagent kit from Invitrogen (cat# 4478359). First, the cultures were centrifuged at 2000 × *g* for 10 min at room temperature to remove cells. Second, the cell-free supernatant was then centrifuged at 10,000 × *g* for 10 min and filtered (0.22 μm) to remove additional cell debris after which 5.0 mL of reagent was added to each tube and incubated overnight at 4°C. These were then centrifuged at 10,000 × *g* for 1 h at 4°C. The pellet was then suspended in 1.0 mL PBS and purified using IZON qEV 35 nm size exclusion column.

2.13 | Nanoparticle Tracking Analysis (NTA)

EVs particle size and concentration from the treated and non-treated samples were determined using NanoSight NS300 instrument (Malvern Instruments, Malvern, UK). First, the samples were diluted 1:100 in PBS. The concentration, average size, size distribution and mode size were then performed using the NanoSight software version 3.4 with a camera level of 13, a video time of 60 s with detection threshold of 5. Three injections and measurements were done for each sample. The data obtained were then plotted using GraphPad Prism with the mean sizes represented as average ± std.

2.14 | Dynamic Light Scattering (DLS)

The purified EVs from the different cell lines were suspended in PBS to a concentration of 50 μg protein/mL, 70 μL was used in the cuvette and analysis were performed with a Zetasizer Nano ZS (Malvern Instruments, Ltd.). Intensity, volume and distribution data for each sample were collected continuously for 4 min in three sets.

2.15 | Transmission Electron Microscopy (TEM)

For morphological analysis, TEM was performed following a previously described protocol by He et al. (2025) with minor modifications. Briefly, 10 μL of EVs (HuT 102 and Jurkat EVs) was applied to Formvar carbon-coated nickel grids and incubated for 1 h at room temperature to allow vesicle adsorption. The grids were then fixed in 2% paraformaldehyde for 10 min, gently washed with PBS, and air-dried. Imaging was performed using a Jeol TEM JEM-1400 transmission electron microscope operated at 80 kV. Random fields were photographed using an 11-megapixel camera system (Quemesa, Olympus, Tokyo, Japan) to assess vesicle size and morphology.

2.16 | Test for Inhibition of Cell-to-Cell HTLV-1 Transmission

Virus-producing cells (MT2 or C91) were co-cultured with reporter Jurkat cells containing the gene encoding luciferase under the control of the HTLV-1 5' LTR viral promoter. Before co-culturing, the HTLV-1- producing cells were inactivated by exposure to mitomycin C (1 μg/10^6cells) for 20 min as previously described (Alais et al. 2017). After that, the cells were washed with PBS and co-cultured with the Jurkat reporter cells. To check if the different EVs (DMSO treated and iTax/PDZ-01 HuT 102) would impact viral transmission,1.6 μg of each EVs were added to the co-culture and read-outs done 48 h later. For microRNA (miRNA) experiments the virus producing cells were first transfected with the different microRNAs (mimic and inhibitors) at different concentrations (0, 3.4, 14, 55 and 222 nM) for 24 h prior to co-culture. For direct inhibition, EVs (1.6 μg) produced from miR-320c mimic or inhibitor were added directly to the co-culture and incubated 48 h. An identical approach was applied to EVs obtained from iTax/PDZ-01 as well as DMSO treated cells. The luciferase activation assay was performed as described above after 24-h incubation.

2.17 | EVs Analysis Using Mass Spectrometry

Proteomic analysis was performed using three biological replicates per condition, with each sample analysed in duplicate (two technical re-injections). For each injection a total of 1 μg of digested protein was injected into the liquid chromatography mass spectrometry (LC-MS/MS) system. LC-MS/MS analyses were conducted using an Acquity M-Class UPLC system (Waters) coupled to either a Q Exactive (for HuT 102 samples) or a Q Exactive Plus (for Jurkat samples) mass spectrometer (Thermo Scientific), operating in nano-electrospray positive ion mode. Chromatographic separation was achieved using a Symmetry C18 trap column (5 μm, 180 μm × 20 mm) and an HSS T3 C18 analytical column (1.8 μm, 75 μm × 250 mm; Waters Corp., Milford, USA). Peptides were loaded onto the trap column at a flow rate of 20 μL/min in 98% solvent A (0.1% formic acid in water) for 3 min. Separation was performed on the analytical column using a linear gradient over 155 min (total run time: 180 min) at a flow rate of 500 nL/min. Solvent B consisted of 0.1% formic acid in acetonitrile. Mass spectrometry parameters were as follows: full MS scans were acquired in the m/z range of 400–1600 with a resolution of 70,000 at m/z 200, an AGC target of 3e6, and a maximum injection time of 200 ms (Q Exactive) or 50 ms (Q Exactive Plus). For MS/MS acquisition, a 2.0 m/z isolation window was used with a normalized collision energy (NCE) of 27 (Q Exactive) or 28 (Q Exactive Plus), resolution set to 17,500 at m/z 200, AGC target of 1e5, and maximum injection time of 50 ms. Raw data files were processed using MaxQuant software (version 2.4.14.0) (Cox and Mann 2008). Variable modifications included deamidation of asparagine/glutamine, N-terminal protein acetylation, and oxidation of methionine, while carbamidomethylation of cysteine was set as a fixed modification. MS/MS spectra were searched against the UniProt human protein database (downloaded 28 February, 2024; 20,433 sequences). For HuT 102 samples, the human database was supplemented with the UniProt HTLV-1 database (downloaded 12 March, 2024; 6041 sequences). A false discovery rate (FDR) of 1% was applied at both peptide-spectrum match (PSM) and protein levels. Protein identification required a minimum of two peptides, including at least one unique and one razor peptide. The precursor mass tolerance for the main search was set at 4.5 ppm. Quantification was performed using label-free quantification (LFQ) with MaxQuant's built-in normalization. Further downstream statistical and bioinformatic analyses were conducted using Perseus software (version 2.0.11) (Tyanova et al. 2016). All data were log2-transformed prior to statistical testing. Differential expression was assessed using a two-sample t-test. Significance thresholds were determined using a permutation-based FDR method (FDR = 5%, s0 = 0.1).

2.18 | miRNA Sequencing of EVs

EVs RNA from treated and non-treated samples was isolated using a Total Exosome RNA and protein kit from Invitrogen, (Cat# 4478545) according to the manufacturer's protocol. The 5200 Fragment Analyzer system was used for RNA quality control (QC) analysis. A cDNA library was constructed from the two sets of samples (EVs from DMSO and iTax/PDZ-01 HuT 102 or Jurkat cells) using QIAseq miRNA Library Kit (QIAGEN, 331502) and the QIAseq miRNA48 IndexIL (QIAGEN,331595). The samples were then sequenced on NovaSeq 6000 sequencer (Illumina, San Diego, CA, USA) using the NovaSeq XP protocol running single-end 100 cycles in a SP flow lane. The raw data were then uploaded to the Qiagen website and mapped using miRBase_v22 with *Homo sapiens* as reference. The differential expression of the miRNAs was then calculated and displayed in volcano plots with the FDR < 0.5 and log2 |fold change| > 1.

2.19 | miRNA Transfection and RT-qPCR Analysis

HuT 102 cells were plated (3×10^5 per well) in 48-well plates and thereafter the cells were transfected with the miRNA mim-

ics purchased from Qiagen using PEI (miR-320c (Cat# 339173 YM00472129-ADA), Negative Control (Cat# 339173 YM00479902-ADA). Other miRNAs (miR-320b, d and e) were purchased from Eurogentec. The miR-320c inhibitor was purchased from MedChemExpress. These were done in triplicates and at four different concentrations (222, 55.5,13.9 and 3.4 nM) for each mimic. The cells were then cultured for 48 h (or 72 h for EV collection) at 37°C and harvested for RNA extraction. Two cDNA kits were used, Fast Gene Scriptase II (Cat# LS63) from Nippon Genetics Europe for genomic cDNA synthesis and miRNA All-In-One cDNA synthesis kit (Cat# G898) from Abm Good. The cDNAs were then used in the RT-qPCR experiments to quantify the expression of human, viral mRNAs and miRNAs. HRPT was used as a reference gene for mRNA expression while U6 was used as a reference for miRNA expressions.

2.20 | Statistical Analysis

The values of the graphs are presented as the mean ± standard deviation, calculated on at least three independent experiments. Significance was determined using a *t*-test and one-way Anova. Normal distribution was checked using Shapiro–Wilk test. The thresholds of p value are represented as follows; * = $p < 0.05$; ** = $p < 0.01$; *** = $p < 0.001$ and **** = $p < 0.0001$

3 | Results

3.1 | A Comprehensive Interactome Map of Tax-1 With Human PDZ-Containing Proteins

Previous studies have demonstrated that the preferred infection route of HTLV-1 is via an infected to a normal T-cell, across a virological synapse that originates from the Golgi apparatus (Cook et al. 2017; Bangham 2000; Nejmeddine and Bangham 2010; Nejmeddine et al. 2009; Barnard et al. 2005; Kimata et al. 1994). An alternative mechanism by which HTLV-1 may enhance its spread is through the release of EVs containing viral transcripts and proteins, which do not initiate de novo infection on their own, but may promote viral replication, enhance transmission efficiency, or modulate the host environment to favour infection (Jaworski et al. 2014; Kim et al. 2021; Anderson et al. 2016). The above processes are highly dependent on the interplay between key host and viral factors, and these interactions should be considered as drug targets. The Tax-1 protein is still viewed as 'undruggable', essentially because of its multiple partners, pleiotropic effects and low expression levels in most HTLV-1-infected cells. Tax-1 can shuttle between cellular compartments and organelles, including EVs whose interactome is yet to be defined. We reasoned that a detailed understanding of the Tax-1 interactome could reveal specific Tax-1 interaction modules, amenable to small molecule inhibition. We have previously highlighted the function of Tax-1 as a hub molecule, capable of interacting with several host cell complexes at the transcription, post-transcription, and translation levels (Vandermeulen et al. 2021; Boxus et al. 2008; Simonis et al. 2012). To date, both high-throughput and small-scale/focused studies have identified 258 human proteins interacting with Tax-1 (Vandermeulen et al. 2021). However, to comprehensively estimate the size of the Tax-1 interactome, we identified potential interacting partners based on motif-domain and domain-domain interactions. As such, we predicted 2401 Tax-1 interactions with human proteins, including 258 experimentally validated PPIs (Figure 1A). This might indicate that about 10% of the full human proteome could potentially be affected by this viral oncoprotein through a well-defined set of interaction modules (Table S1).

In order to understand the functional plasticity of the Tax-1 interactome, we hypothesized that transient associations controlled by multi-domain scaffolding proteins are able to dynamically relocate Tax-1 complexes within the cell, as demonstrated for binary interactome yeast models (Lambourne et al. 2021; Fakhar et al. 2023; Van Criekinge and Beyaert 1999). In the context of Tax-1 and its re-localization in EVs, human PDZ-containing proteins are ideal targets because the vast majority of them are hub proteins with several intracellular and intercellular partners (Table S2) located in different compartments where Tax-1 exerts its disruptive functions (Vandermeulen et al. 2021). To generate the comprehensive interactome of Tax-1 with human PDZ-containing proteins, we combined three different sources of Tax-1 PPI datasets (Figures 1B and S1A), including (i) literature-curated high quality interactions (Figure S1B), (ii) systematic yeast two-hybrid interactions obtained by testing a library of 248 individual PDZ domains and orthogonally validated using the Gaussia princeps complementation assay (GPCA) (Cassonnet et al. 2011) and (iii) GST-pulldown analyses of open reading frames (ORFs) available in the human ORFeome collections (http://horfdb.dfci.harvard.edu/hv7/) (Figure S1C–E). Our approach allowed us to generate a Tax-PDZ interactome (Figure 1B) encompassing 54 human proteins. This represents 36% of the entire human PDZome (Amacher et al. 2020), and a substantial increase from the 14 already known human PDZ proteins directly interacting with Tax-1 (Figure S1B).

To further determine the relative implication of PDZ-containing proteins in the human interactome, we used the human binary reference interactome map (HuRI) (Luck et al. 2020) and ranked PDZ proteins according to their number of direct interactors ('first degree' or proteins interacting with Tax-1 partners) or indirect associations ('second degree') (Table S2). The average number of first- and second-degree Tax-1 partners represent 24 and 536 PPIs, respectively, further emphasizing the scaffolding role of PDZ-containing proteins targeted by the viral Tax-1 oncoprotein.

To assess the overall biological significance of the Tax-PDZ interactome, we compared our new dataset with transcriptomic and genomic data of human PDZ protein-coding genes in different relevant datasets: (i) expression data across 24 different T-cell lines (Figure 1C, Table S3); (ii) differential expression data in HTLV-1-infected versus non-infected cells (Figure 1D, Table S3); (iii) differential expression data in Jurkat cells expressing Tax-1 versus control cells (Figure 1E, Table S3); (iv) mutational landscapes in ATL patient samples (Figure 1F, Table S3) and (v) transcriptome data from a 'gene signature' of ATL (Bazarbachi 2016; Fujikawa et al. 2016) (Figure 1G). Taken together, this comprehensive analysis highlights the implication of PDZ genes and their products in the biology of HTLV-1. Finally, we performed a spatial analysis of functional enrichment (SAFE) (Baryshnikova 2016) using the above datasets and a STRING network of Tax-1/PDZ interactors (Table S2). We identified five significantly enriched biological processes, including nucleic acid

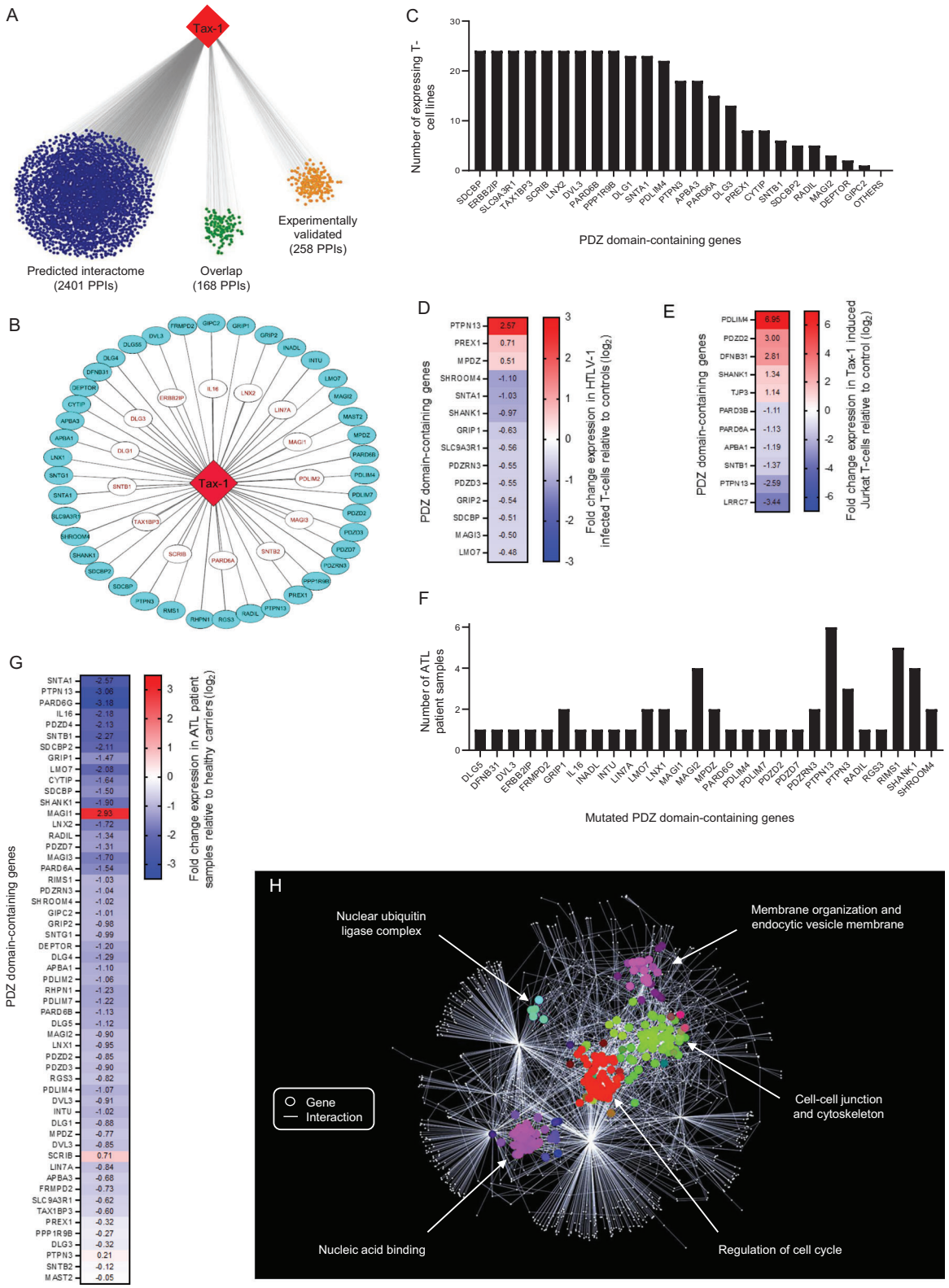

FIGURE 1 | **A comprehensive analysis of the Tax-1 interactome with human PDZ containing proteins.** (**A**) *In silico* prediction of interactions between Tax-1 domains and motifs and human protein domains listed in Table S1. (**B**) A map of Tax-1-PDZ interactome. Red indicates overlap with PPIs known from the literature. (**C**) Expression of the interacting PDZ-containing protein genes across 24 different T-cell lines. (**D**) Differential expression data in HTLV-1-infected versus non-infected T-cells (genes for which $p < 0.05$ are shown). (**E**) differentially expressed PDZ genes in Jurkat T-cells following induction of the Tax-1 expression (genes for which $p < 0.01$ are shown). (**F**) PDZ genes mutated in ATL patient samples. (**G**) Differentially expressed PDZ genes in ATL patient samples relative to healthy carriers (genes for which $p < 0.05$ are shown). (**H**) SAFE analysis of the Tax-1/human PDZ proteins interactome. See also Figure S1, Table S1.

binding, nuclear ubiquitin-binding, regulation of cell cycle, cell–cell junction and cytoskeleton organization, and endocytic vesicle membrane assembly (Figure 1H). The identified observations strongly suggest that PDZ proteins might be privileged association partners for Tax-1, allowing the viral protein to target multiple cellular processes, which may be needed for the viral functions at different disease progression stages.

3.2 | A Structural Analysis of Tax-1/Syntenin-1 PDZ Interactions

The above SAFE analysis highlighted endocytic vesicle membrane assembly as one of the enriched functions in the Tax-1/PDZ interactome (Figure 1H). The subnetwork of this function highlights syntenin-1, also known as SDCBP, which has the highest connectivity in this subnetwork (Figure S2A) and also in the human reference interactome map(HuRI (Luck et al. 2020), http://www.interactome-atlas.org/). To determine the structural basis of Tax-1/syntenin-1 interaction, we employed solution NMR spectroscopy. Monitored in a series of [^{1}H,^{15}N] heteronuclear single quantum correlation (HSQC) experiments, binding of the natural-abundance, NMR silent *C*-terminal Tax-1 decapeptide (Tax-1 10-mer) to the ^{15}N labelled, NMR-visible PDZ1, PDZ2 or tandem PDZ1+2 domains of syntenin-1 causes large spectral changes (Figure 2). Addition of Tax-1 10-mer to ^{15}N syntenin-1 PDZ1+2 leads to incremental chemical shift changes for some of the resonances, several of which progressively disappear in the course of the titration, which is symptomatic of the fast-to-intermediate NMR exchange regime. The chemical shift perturbations map to the canonical peptide binding sites of both PDZ1 (including residues I125 and G126) and PDZ2 (residues V209, G210, F211 and F213) domains, encompassing the $\beta1/\beta2$ loop, the $\beta2$ strand, and the $\alpha2$ helix (Figure 2A). The binding effects are stronger for the PDZ2 domain and appear to extend to the back of the protein (including residues T200, L232 and T266) (Figure 2A,B). These findings are consistent with an earlier study of syntenin-1-peptide interactions by x-ray crystallography that highlighted a binding-induced reorientation of the $\alpha2$ helix (Grembecka et al. 2006), which could explain the chemical shift perturbations of the residues at the back of PDZ2 (Figure 2B).

To evaluate the binding contribution of each PDZ domain, we performed NMR experiments with the Tax-1 10-mer and individually expressed syntenin-1 PDZ1 and PDZ2 domains. Overall, the chemical shift perturbation maps for isolated PDZ1 (Figure 2C–E) and PDZ2 (Figure 2F–H) are similar to those for the PDZ1+2 tandem (Figure 2A, B). A slight preference for the PDZ2 domain is observed, with K_D values of 2.6 and 1.6 mM for PDZ1 and PDZ2, respectively (Figure 2E, H). Furthermore, NMR experiments with the Tax-1 PBM 4-mer and the control N-terminal 6-mer (lacking PBM) peptides illustrate that the four C-terminal residues of Tax-1 (ETEV) are necessary and sufficient for the interaction with the syntenin-1 PDZ1 and PDZ2 domains (Figure S2B–D). We further show through fluorescence polarization (FP) that the syntenin-Tax-1 interaction is facilitated by the PBM as evidenced by non-interaction with Tax-2 (Figure S2E)

3.3 | A Crosstalk Between Tax-1/PDZ Interaction and Membrane Vesicle Trafficking

We first tested if a small molecule known to bind to syntenin-1, syntOFF (Leblanc et al. 2020) would disrupt HTLV-1 Tax-1/syntenin-1 interaction and block viral cell-to-cell transmission. Interestingly, the compound indeed showed inhibition in our co-culture experiments and fluorescence polarization (FP) assays (Figures S3A–C and 3B). The inhibition was lower compared to another small molecule, iTax/PDZ-01, which we recently reported for the inhibition of hDLG1-Tax-1 interaction and previously referred to as 'compound **3**' (Maseko et al. 2023). This result then prompted us to check if iTax/PDZ-01 would bind to syntenin-1 and inhibit its interaction with Tax-1 PBM. Indeed, the compound showed a concentration dependent decrease in FP and viral cell-to-cell transmission (Figures 3A,B and S3A–C). Syntenin-1 is particularly relevant for viral infections as it is a well-characterized exosome marker (Lim et al. 2021) controlling EVs formation and cell-to-cell communication (Leblanc et al. 2020; Lim et al. 2021; Imjeti et al. 2017). Although Tax-1 has been shown to localize into EVs from HTLV-1 infected cells and contribute to viral spread and disease progression (Al Sharif et al. 2020; Pinto et al. 2019), the molecular mechanisms controlling Tax-1 recruitment into EVs are unknown.

As syntenin-1 is involved in EVs biogenesis, we then hypothesized that a small molecule binding to syntenin-1 would also affect Tax-1 in EVs, thereby reducing cell-to-cell viral transmission. We thus evaluated EVs from HTLV-1 producing cells (HuT 102) cultured in the presence or absence of the small molecule iTax/PDZ-01. Cells were cultured in medium supplemented with 10% EVs-free FBS and treated with 25 μM of iTax/PDZ-01 (25 μM is an estimate of the IC_{50}, and has low toxicity) (Figure 3C). Analysis of the average sizes of the EVs using NTA showed larger sizes from the control than the treated cells (181.6 ± 2,7 nm and 154 ± 4,4 nm, respectively) (Figure 3D). We further confirmed that the samples indeed contained EVs by performing TEM (Figure 3E).A similar effect was observed when treating other HTLV-1 infected cells with the same small molecule (Figure 3F). The EVs were indirectly controlled by the amount of calnexin in the EVs sample using western blot (Figure 3G–H). There was a drastic decrease in syntenin-1 levels in both cells and EVs when treated with the small molecule, as evidenced by immunoblotting (Figure 3G–H). Interestingly the reduction in syntenin-1 led to a concomitant decrease in Tax-1 levels as well, suggesting that both proteins form a complex in the EVs of infected cells (Figure 3H). To validate whether the effects of iTax/PDZ-01 observed in infected HuT 102 cells could be recapitulated in non-infected cells, we treated Jurkat cells with the compound and performed EV characterization following the same workflow. Western blot analysis of EV protein cargo showed a reduction in syntenin-1 levels following iTax/PDZ-01 treatment; however, the extent of this decrease was notably less pronounced than in EVs from infected cells (Figure S3D). Nanoparticle tracking analysis revealed that EVs derived from iTax/PDZ-01-treated Jurkat cells exhibited a modest increase in particle size compared to DMSO-treated controls (Figure S3E), although the overall size distribution was

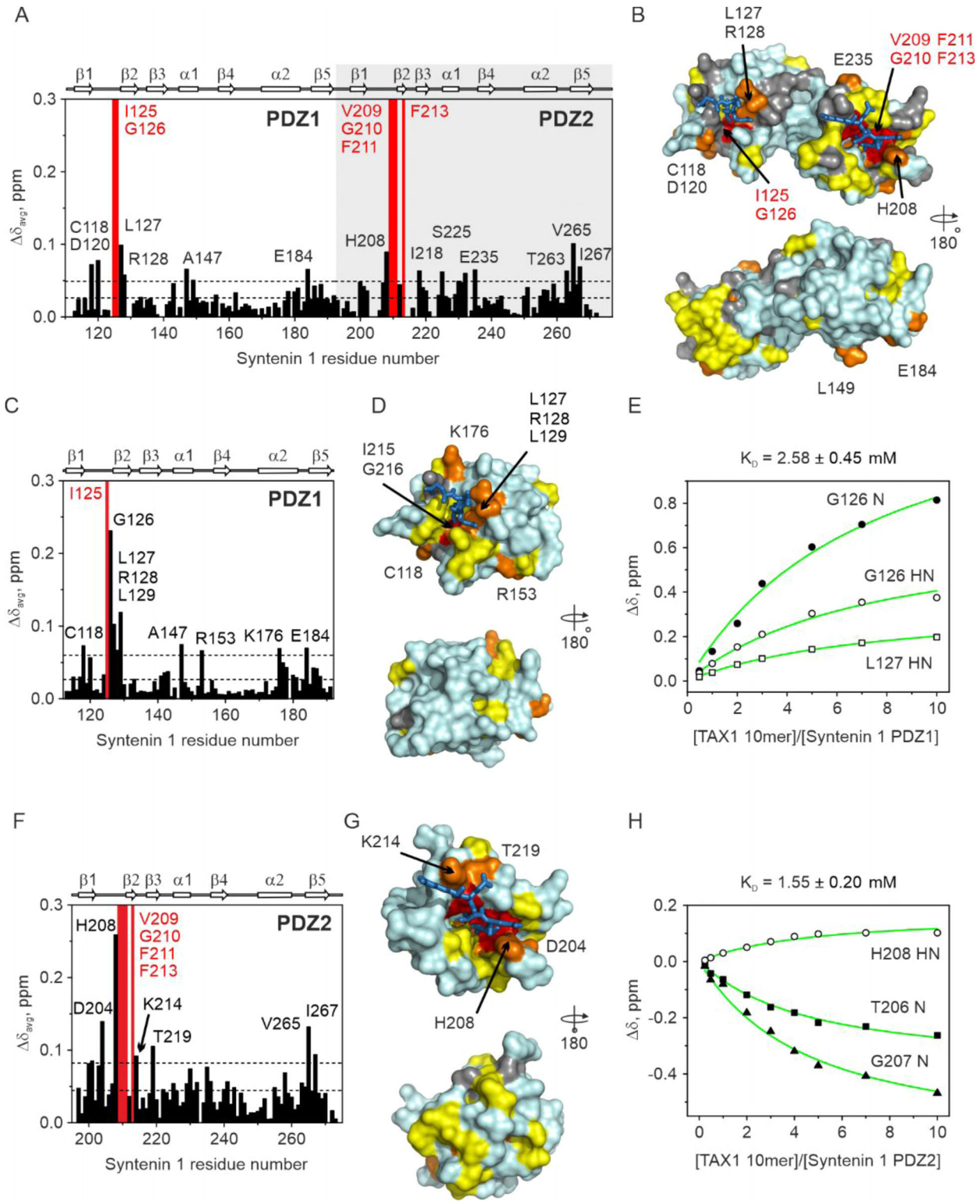

FIGURE 2 | **NMR-observed binding of the Tax-1 10mer peptide to syntenin-1 PDZ domains**. The interaction of Tax-1 10mer with ^{15}N syntenin-1 (**A**--**B**) PDZ1+2 tandem or individual (**C**–**E**) PDZ1 and (**F**–**H**) PDZ2 domains. **A, C, F** $\Delta\delta_{avg}$ in the presence of five molar equivalents of Tax-1 10mer. Residues with backbone amides broadened beyond the detection limit upon complex formation are indicated by red bars. The horizontal lines show the average $\Delta\delta_{avg}$ and the avg + stdev. Residues with large $\Delta\delta_{avg}$ are labelled. The secondary structure of syntenin-1 PDZ1 and PDZ2 domains, drawn from the PDB entry 1W9E (Grembecka et al. 2006), is shown above the plot. (**B, D, G)** Chemical shift mapping of the Tax-1 10mer binding. The molecular surfaces of syntenin-1 PDZ domains are coloured by the $\Delta\delta_{avg}$ values (yellow: $\Delta\delta_{avg}$ > avg; orange: $\Delta\delta_{avg}$ > avg + stdev; red: broadened out upon binding). Prolines and residues with unassigned or strongly overlapping backbone amide resonances are in grey. The modelled C-terminal parts of the Tax-1 peptide, bound to the canonical PDZ sites, are shown in sticks. (**E, H)** NMR chemical shift titrations with the Tax-1 10mer peptide. Chemical shift perturbations of the backbone amide atoms indicated in the plots were fitted simultaneously to a binding model with the shared K_D (Equation 1). The solid lines show the best fits with (E) $K_D = 2.58 \pm 0.45$ mM for syntenin-1 PDZ1 and (H) $K_D = 1.55 \pm 0.20$ mM for syntenin-1 PDZ2.

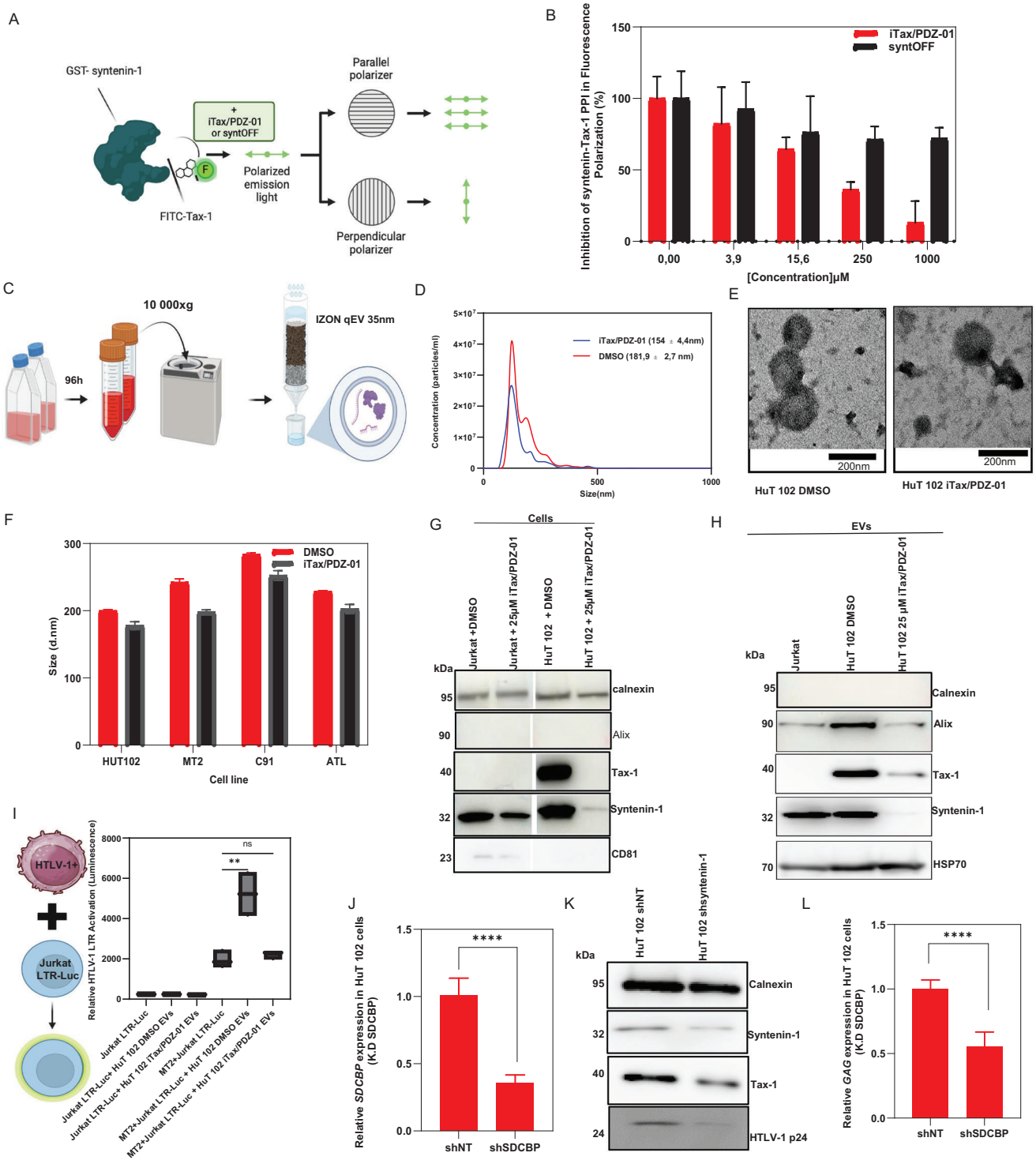

FIGURE 3 | Inhibition of HTLV-1 Tax-1/syntenin protein-protein interaction with small molecule and its effect on EVs. (**A**) Schematic representation of fluorescence polarization (FP). (**B**) Inhibition of Tax-1/syntenin interaction in FP using syntOFF and iTax/PDZ-01. (**C**) schematic representation of EVs extraction and purification from HUT 102 treated with DMSO or iTax/PDZ-01. (**D**) NTA analysis of EVs from DMSO and iTax/PDZ-01 treated HuT 102 cell lines. (**E**) Representative TEM scale bar on images of EVs released from DMSO and iTax/PDZ-01 HuT 102 cells showing the presence of EVs around 200 nm in diameter: scale bar = 200 nm. (**F**) Average sizes of EVs from 4 HTLV-1 producing cells from DLS analysis treated with DMSO or iTax/PDZ-01. (**G**), Western blot analysis of DMSO and **iTax/PDZ-01** Jurkat and HuT cells HuT 102 cells. (**H**) Effect of **iTax/PDZ-01** on proteins in EVs. (**I**) Role of exosomes in viral transmission, MT2 cells were co-cultured with Jurkat-LTR-Luc reporter cell line and then treated with 1.6 µg EVs. Luciferase activity was then quantified 24 h later. (**J**) Analysis of SDCBP (syntenin-1) knockdown in HuT 102 cells using RT-qPCR. (K) The effect of SDCBP knockdown in HuT 102 (protein level). (**L**) Quantification of viral particles in SDCBP knockdown cells using RT-qPCR. The data points in the bar graphs represent the mean ($n = 3$); the errors are standard deviations from the mean. Statistical significance was determined with a one-way ANOVA for **I** and unpaired *t*-test for **K** and **L** (*$p < 0.05$, **$p < 0.01$, ***$p < 0.001$ and ****$p < 0.0001$) in GraphPad Prism.

similar to that observed in HuT 102-derived EVs. This was further confirmed by TEM where we see similar sizes as the infected cells (Figure S3F–G). These results suggest that while iTax/PDZ-01 modulates syntenin-1 levels in both infected and uninfected cells, the effect is more substantial in the context of HTLV-1 infection. EVs from HTLV-1 producing cells were shown to promote cell-to-cell HTLV-1 transmission (Pinto et al. 2019). We therefore tested whether compound-treated cells could be impaired in their ability to support cell-to-cell viral transmission. EVs from DMSO treated HuT 102 cells showed a significant increase in viral transmission compared to co-culture not treated with EVs from HTLV-1 infected cells. This was in turn abolished when EVs were isolated from cells treated with the small molecule (Figure 3I). Having seen that EVs from treated cells show lower levels of syntenin-1, we wondered if knocking down syntenin-1 in HTLV-1 positive cells, HuT 102, would have an impact on viral replication. We observed a significant decrease in HTLV-1 *GAG* mRNA following syntenin-1 knockdown as determined by RT-qPCR. There was similar observation at protein level as well as seen from the western blot, which emphasizes the link between syntenin-1 and HTLV-1 *GAG* expression (Figure 3J–L).

3.4 | A Comparative Proteomic Analysis of EVs

The effect of the EVs in viral transmission prompted us to check the protein content of EVs from control and iTax/PDZ-01-treated cells using mass spectrometry. Principal Component Analysis (PCA) shows that samples cluster clearly by condition, demonstrating high reproducibility among biological replicates and distinct separation between groups (Figure S4A, B). We then investigated the global effect of the small molecule on both HTLV-1 and EV proteins. There were 428 differentially abundant (DA) proteins in the EVs (Figure 4A, Table S4). Proteins known to be dysregulated in HTLV-1 or cancer cells are highlighted, as well as those with higher fold changes compared to the control. Among the most down regulated proteins was LGALSBP (lectin galactoside-binding soluble 3 binding protein), which was reduced by more than 200-fold compared to the control. This protein has been shown to be upregulated in cancer patients as well as people infected by HIV (Capone et al. 2021). Another example is CD70 which was shown to be upregulated by 1000-fold in HTLV-1 infected cells (Human 2008) and this high expression level has been linked to Tax-1. Interestingly CD70 levels in EVs isolated from compound-treated cells was significantly reduced due to lower Tax-1 levels (Figure 4A). The proteins of the tetraspanin superfamily (which includes CD63, CD81 and CD82 among others) are also less abundant in EVs from treated cells, and they are crucial for the structure of membrane protein complexes, the regulation of T cell adhesion and the regulation of integrin activity (Mazurov et al. 2007). They also play a role in viral transmission by making direct contacts with viral proteins, for instance CD82 can bind to the HTLV-1 Gag protein (Mazurov et al. 2007). CD81 on the other hand has been recently shown to interact with syntenin-1 through its PBM (Castro-Cruz et al. 2023). Both the levels of CD81 and CD82 were significantly reduced in the EVs of treated cells (Figure 4A). There was a 12-fold reduction in the syntenin-1 levels due to treatment with the small molecule (Figure 4A). The lower syntenin-1 level in the treated samples correlates with the reduction in viral proteins as evidenced by the Gag-Pro-Pol, Gag and Tax-1 levels. HTLV-1 proteins identified in this study are shown in Figure 4B. SPEED2 (Parikh et al. 2010) (Figure 4C) signalling pathway enrichment analysis revealed that iTax/PDZ-01 treatment in HuT 102 cells was associated with the activation of key polarity- and trafficking-related signalling pathways, including Wnt, Notch, Hippo, and MAPK–PI3K. These pathways are tightly regulated by PDZ-domain scaffolding proteins such as syntenin-1, DLG1, SCRIB and others, which play essential roles in organizing protein complexes involved in cell polarity, endosomal sorting, and EV biogenesis (Baietti et al. 2012; Santoni et al. 2020). Activation of MAPK–PI3K may also reflect a stress-adaptive or compensatory response to the disruption of PDZ-dependent intracellular signalling hubs (Jørgensen 2005). Notably, we observed minimal changes in inflammatory and innate immune signalling pathways, such as TLR, TNFα, IL-1 and JAK-STAT, suggesting that iTax/PDZ-01 does not provoke broad pro-inflammatory activation, which is favourable in the context of therapeutic development. To further investigate the effects of iTax/PDZ-01 in a non-infected context, we performed quantitative proteomic analysis of EVs derived from Jurkat cells treated with the compound. Differential abundance (DA) analysis identified a subset of proteins whose expression overlapped with those altered in EVs from iTax/PDZ-01-treated HuT 102 cells. Specifically, approximately 37% of the DA proteins in Jurkat EVs were also differentially abundant in HuT 102 EVs (Figure S4DE, Table S4). However, the magnitude of fold changes in these shared proteins was consistently lower in Jurkat cells. For example, syntenin-1, a key target of the compound, exhibited a 4-fold reduction in Jurkat-derived EVs, in contrast to a 12-fold decrease observed in EVs from HuT 102 cells (Figure S4D). These findings suggest that while iTax/PDZ-01 influences similar molecular targets in both infected and non-infected cells, the presence of HTLV-1 infection amplifies the compound's effects on EV protein composition. Again, SPEED pathway analysis showed similar pathways as the HuT 102 cells (Figure S4E). We then performed Gene Ontology analysis on the downregulated HuT 102 EV proteins and performed PPI enrichment evaluations. Interestingly, most of the clusters showed extracellular matrix or cytoskeleton organization as being the most enriched pathways (Figure 4D), which agrees with our SAFE analysis (Figure 1H). Pathway and process enrichment analyses performed on the up-regulated proteins showed completely different results, highlighting involvement of other cellular processes, including ribosome functions and nucleotide metabolism (Figure S4F). We finally expanded our investigation into the syntenin-1 interactome to examine the impact of the small molecule on primary and secondary interactors (Figure 4E). We identified 23 direct interactors of syntenin-1, although only four proteins were significantly differentially abundant in response to the small molecule, including RNA binding proteins (RBPs) SUB1, SRSF11 and SRSF3.

3.5 | A Reprogramming Strategy of EV microRNAs (miRNAs)

We next characterized the miRNA content of EVs from iTax/PDZ-01-treated or control HuT 102 HTLV+ cells by RNAseq. There were 288 differentially abundant miRNAs, 121 were down regulated and 167 were upregulated by the small molecule compared to the control condition. The overall miRNAs identified are listed in Table S5. To link these miRNAs to gene targets, we used the

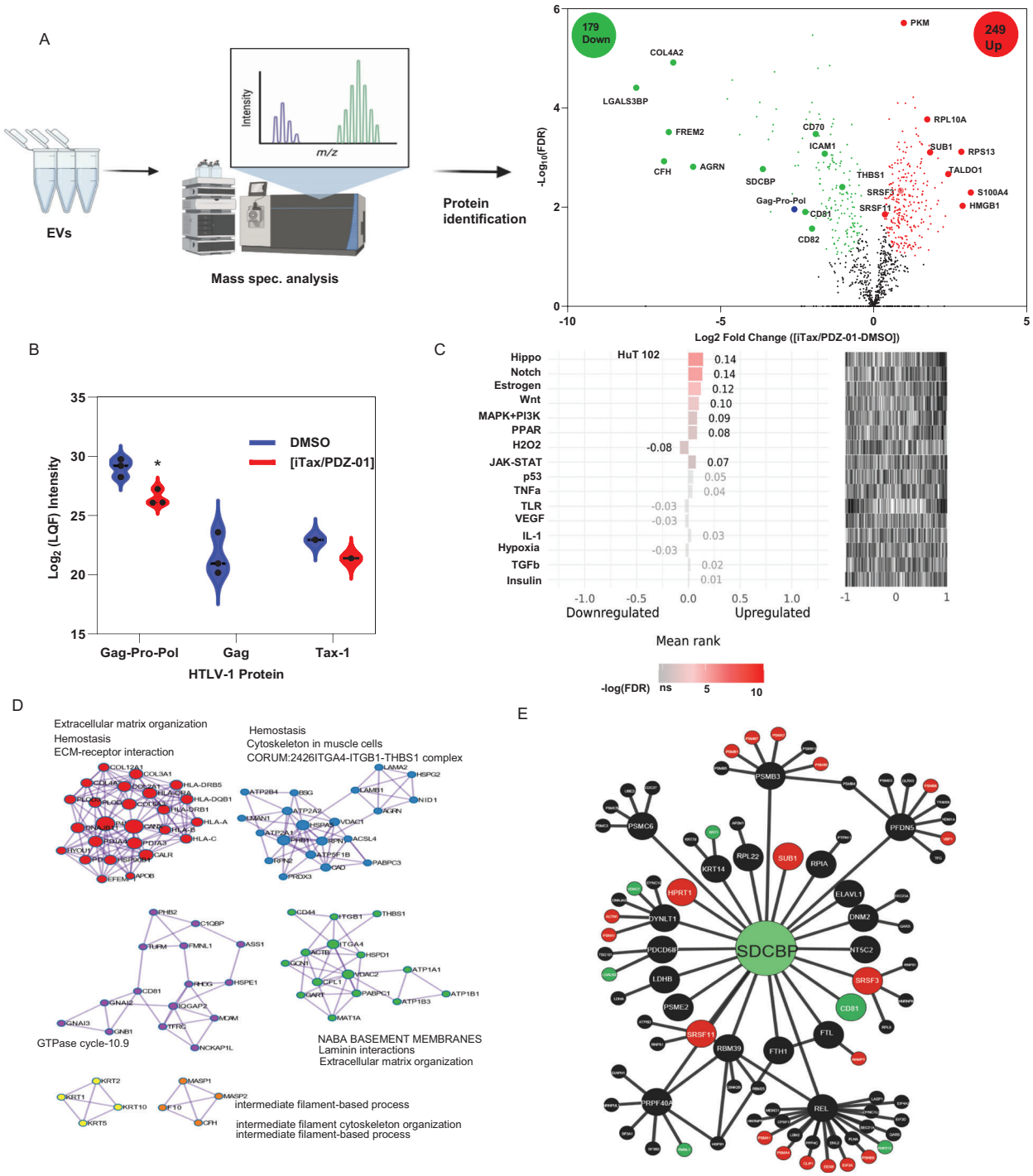

FIGURE 4 | **Mass spectrometry analysis of EV proteins from treated and non-treated EVs from HuT 102 cells**. (**A**) Schematic representation of mass spectrometry and a volcano plot showing all proteins identified in the two sets of EVs, there were 428 differentially expressed (DE) proteins, down regulated proteins are shown in green and up regulated are in red. Proteins targeted by HTLV-1 are highlighted. (**B**) Violin plot of HTLV-1 proteins determined in the two sets of samples. (**C**) **Signalling pathway activation was analysed using the SPEED online tool**. The x-axis displays z-scores ranging from −1 to 1, indicating the relative ranking of upregulated and downregulated genes across different pathway experiments. Bar graph heights represent the mean rank of the query gene list for each pathway, while bar colours correspond to adjusted *p* values. On the right, a barcode plot illustrates the distribution of the query genes, with each black bar indicating the presence of a gene. The statistical significance of mean rank shifts across pathways was assessed using the Bates test. (**D**) Protein–protein Interaction Enrichment Analysis of down regulated genes. Molecular Complex Detection (MCODE) algorithm was applied to identify densely connected network components and to each cluster, pathway and process enrichment analysis was performed. The size of the node represent degree; this was done through Metascape (htt://metascape.org). (**E**) Cytoscape image of primary (big nodes) and secondary (smaller nodes) SDCBP (syntenin-1) interactors, proteins significantly upregulated are shown in red, those significantly downpregulated are shown in green and those that were not significantly affected by the treatment are shown in black. Statistical significance in (**A**) and (**B**) was determined with a *t*-test was performed. The significance threshold was determined using permutation-based FDR implemented in Perseus with a FDR of 5% and a s0 parameter of 0.1*.

Ingenuity Pathway Analysis (IPA, Qiagen). Because miRNAs are linked to many targets, we limited our analysis to the candidate miRNAs targeting proteins identified in the same EVs (Figure 4A, Table S5). Restricting our analysis to experimentally-validated human miRNAs playing a role in T-cell or cancer biology, we found 18 miRNAs linked to 23 human protein targets differentially abundant in the same EVs (Table S5), including 12 miRNAs and 14 EV proteins whose expressions were opposite (Figure 5A, Table S5). GO analysis (Biological process, molecular function and cellular components) on the 14 targeted proteins showed the same enriched pathways (extracellular matrix, cytoskeleton and cell adhesion), as observed in the down-regulated proteins in our proteomic analysis (Figure S5A), suggesting that the small molecule iTax/PDZ-01 can modulate the way HTLV-1 infection affects EV molecular composition. In parallel with the proteomic analysis, we performed small RNA sequencing to evaluate the effect of iTax/PDZ-01 on miRNA cargo in EVs from non-infected Jurkat cells. A total of 86 differentially abundant (DA) miRNAs were identified in EVs from treated Jurkat cells (Figure S5J). Notably, 70% of these miRNAs overlapped with those altered in EVs derived from iTax/PDZ-01-treated HuT 102 cells, suggesting a conserved yet attenuated miRNA response in the absence of viral infection (Figure S5K). Despite this overlap, the magnitude of expression changes in Jurkat EVs was considerably lower. None of the differentially abundant miRNAs exceeded a 10-fold change in expression, indicating a relatively modest impact of iTax/PDZ-01 on the Jurkat miRNA landscape. Interestingly, among the upregulated miRNAs in both cell types was the miR-320 family, with miR-320c showing a 3.5-fold increase in Jurkat EVs compared to the striking 64-fold increase in HuT 102 EVs. This suggests that although iTax/PDZ-01 induces similar regulatory miRNA programs in both infected and uninfected contexts, HTLV-1 infection may potentiate the compound's ability to modulate EV-associated miRNA expression.

Furthermore, several miRNAs reported to be dysregulated following HTLV-1 infection (Machado et al. 2022) were also found in this study (Figure 5B). For example, miRNAs miR-142-3p (which is involved in hematopoietic stem cells formation and favours T-cell differentiation) and miR-146b-5p (which regulates innate immunity) have been shown to be, respectively, up- and down-regulated in HTLV-1 cells. Those effects were reversed by treating the infected cells with iTax/PDZ-01 (Figure 5B). Another interesting example is miR-34 family that exhibits tumour suppressor effects across various cancers (Fawzy et al. 2024), synergizing with p53. Members of miR-34 family have also been implicated in regulation of T-cell activation (Amaral et al. 2017), and are often down-regulated in different virus-infected cells (Amaral et al. 2017; Du et al. 2020; Sommerova et al. 2019). Our results indicate that the iTax/PDZ-01 small molecule increases miR-34a-5p by 5-fold (Figure 5B), suggesting a potential antiviral activity.

3.6 | A Connection Between miR-320 Family and Tax-1/Syntenin-1

Several miRNAs already known to target syntenin-1 were differentially abundant in EVs following the treatment of HuT 102 cells with the iTax/PDZ-01 small molecule (Figure S5B). However, we were intrigued by miR-320 family whose members miR-320c and -320d, were the most significantly upregulated following treatment with the small molecule, by 63- and 62-fold changes, respectively, compared to the control. (Figure 5C). A similar effect was observed from cells treated with iTax/PDZ-01 where we saw a concentration dependent increase in miR-320c and a reduction in viral expression (Figure S5D, E). We then checked if using a mimic would influence syntenin-1 and, importantly, exert an antiviral activity. HuT 102 cells were transfected with the miR-320c and a negative control mimic. We next quantified the mRNA expression 48 h post-transfection using RT-qPCR and observed a concentration dependent decrease in the expression of *SDCBP* mRNA compared to the negative control (Figure 5D). Interestingly there was also a concentration decrease in the *GAG* mRNA indicating an antiviral activity for the miR-320c mimic compared to the control (Figure 5E). Next, miR-320c mimic was used in a cell-to-cell transmission assay, to assess if it could block viral transmission. To this end, MT2 cells were transfected with increasing concentrations of miR-320c, and 24 h later, the cells were co-cultured with the Jurkat-LTR-Luc reporter cell line and incubated for another 24 h. Interestingly, miR-320c reduced viral transmission in a concentration dependent manner (Figure 5H). The same was observed when another HTLV-1 infected cell line, C91 (Figure S5C) was used. The C91 co-culture (although known to have more viral particles and higher infectivity compared to MT2) showed more sensitivity to the miR-320c mimic. This is consistent with the observation we made when using iTax/PDZ-01. We also tested other members of the miR-320 family, including miR-320b, d and e. Only miR-320d and miR-320e showed reduction in *GAG* mRNA expression without affecting the mRNA levels of *SDCBP* (Figure S5F–I). To further investigate the role of miR-320c in regulating HTLV-1 transmission, HuT 102 cells were transfected with a miR-320c inhibitor to suppress its expression. RT-qPCR analysis revealed a concentration-dependent increase in both *SDCBP* and *GAG* transcript levels following inhibition of miR-320c (Figure G–H). Consistent with these findings, Western blot analysis confirmed elevated syntenin-1 protein levels in cells treated with the inhibitor, while mimic-transfected cells showed reduced levels. To determine whether these changes in miR-320c expression influenced viral transmission via EVs, EVs were isolated from mimic- and inhibitor-treated HuT 102 cells and used in a co-culture assay, as described previously. Notably, EVs derived from miR-320c inhibitor-treated cells enhanced HTLV-1 transmission, whereas EVs from miR-320c mimic-treated cells suppressed viral transmission (Figure 5J). Altogether, our results suggest that the small molecule iTax/PDZ-01 is able to inhibit the Tax-1/syntenin-1 interaction while promoting expression of miR-320c, which is able to maintain low levels of *SDCBP* and viral mRNAs in EVs, and consequently reduce viral transmission.

4 | Discussion

One of the strategies used by viruses, including HIV-1 and HTLV-1 retroviruses, to spread from an infected to a non-infected cell, is by establishing virological synapses, which are in some cases preferred routes of transmission of viral materials from a donor to a target cell (Igakura et al. 2003; Galloway et al. 2015). Transferred viral RNAs and proteins can also be encapsulated in EVs such as exosomes, which facilitates viral transmission. They are also associated with disease phenotypes in the absence of complete viral particles (Pokhrel et al. 2024; Jaworski et al. 2014). In this study we characterized the Tax-1 interactome with human PDZ

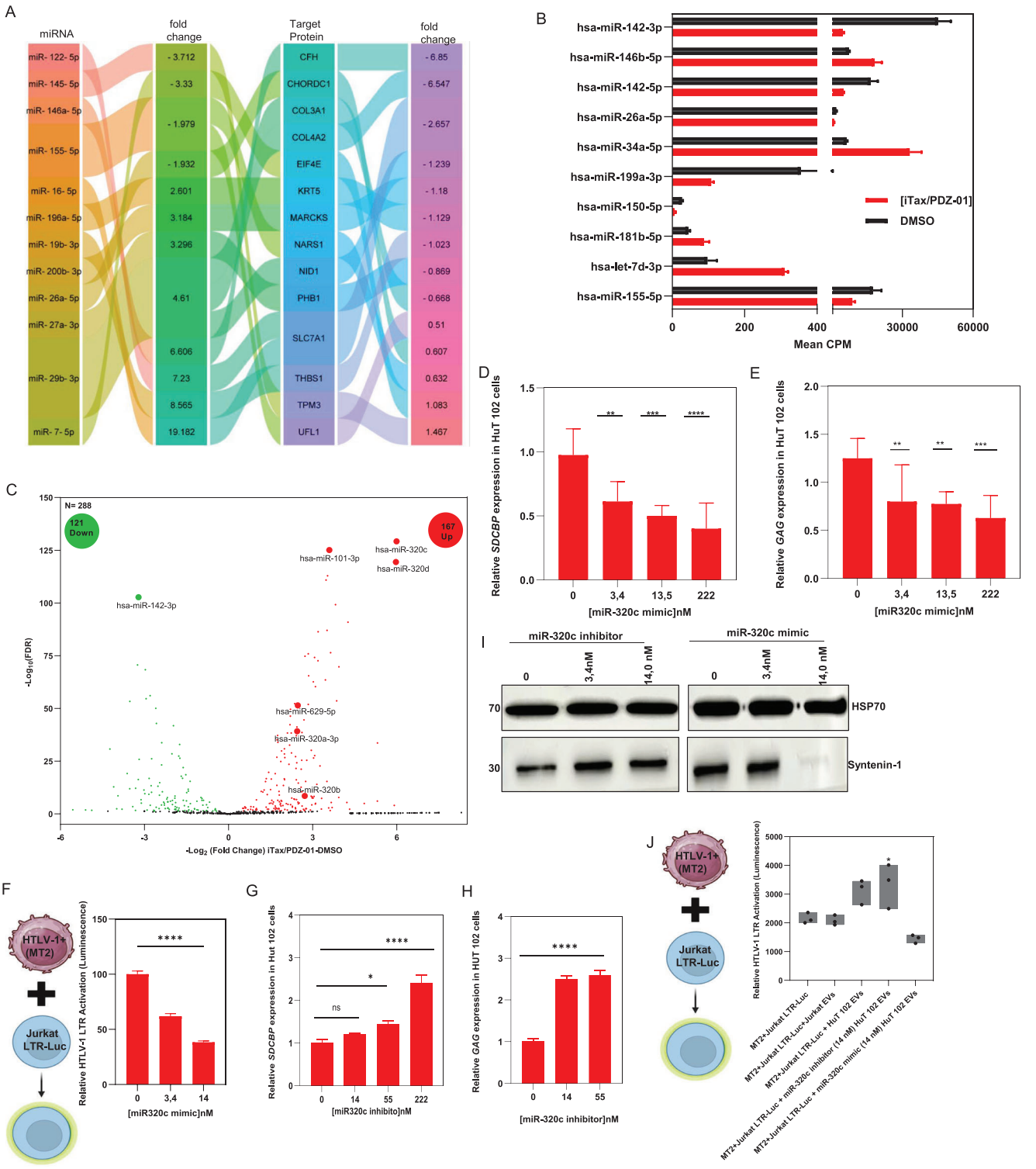

FIGURE 5 | miRNA analysis of extracellular vesicles from treated and non-treated HuT 102 cells and the effect miR-320 family in HTLV-1 viral transmission. (**A**) An alluvial plot showing miRNAs and their gene targets from mass spectrometry with opposite expression obtained using IPA (Qiagen), (**B**) a closer look for miRNA already reported for HTLV-1. (**C**) Volcano plot showing all the miRNA determined, downregulated miRNAs are shown in green, up regulated are shown in red, and those not significantly affected are shown in black in HuT 102 EVs. (**D**) Evaluation of SDCBP (syntenin-1) expression following transfection with miRNA 320c mimic, this was done in four-point concentrations (0, 3.4, 13.5 and 222 nM). (**E**) Relative HTLV-1 *GAG* expression following miR 320c mimic transfection. (**F**) Inhibition of cell-to-cell viral transmission following treatment with miR-320c mimic. (**G**) The effect of miR-320c inhibitor on *SDCBP* in HuT 102 cells. (**H**) Quantification of *GAG* in HuT 102 following treatment with miR-320c inhibitor as a measure of viral numbers by RT-qPCR. (**I**) Western blot analysis of the effect of miR-320c inhibitor and mimic on syntenin-1 at protein level. (**J**) The effect of EVs produced from miR-320c inhibitor and mimic treated HuT 102 cells on viral transmission. The data points in the bar graphs represent the mean ($n = 3$); the errors are standard deviations from the mean. Statistical significance was determined with a one-way ANOVA (*$p < 0.05$, **$p < 0.01$, ***$p < 0.001$ and ****$p < 0.0001$) in GraphPad Prism.

proteins, and how the interaction between Tax-1 and syntenin-1, a scaffold PDZ protein involved in the formation and uptake of exosomes (Kashyap et al. 2021), influences viral transmission.

By testing 248 out of 271 PDZ domains identified in 151 human proteins, our results establish a comprehensive Tax-1/PDZ interactome, highlighting a set of 54 PDZ-domain-containing proteins. Tax-1 binds to PDZ proteins using a conserved *C*-terminal PBM motif, which is lacking in Tax-2 encoded by HTLV-2, highly related to HTLV-1 but not associated with leukemogenesis (Sieburg et al. 2004). A correlation between the presence of a PBM and viral pathogenicity has also been demonstrated for other viruses, independently of their substantial differences in genome structures (RNA and DNA viruses) or modes of infection (acute and persistent families of viruses) (Caillet-Saguy et al. 2021; Caillet-Saguy and Wolff 2021; Jimenez-Guardeño et al. 2014), suggesting that comparative analyses of viral proteins-PDZ interactomes may guide the design of potential broad-spectrum antivirals targeting key host proteins. To validate syntenin-1 as a potential therapeutic target in HTLV-1-induced diseases, we performed a structural analysis showing that a peptide corresponding to the C-terminal segment of the Tax-1 protein binds PDZ1 and PDZ2 domains of syntenin-1. This Tax-1 10-mer engages the canonical peptide binding sites of both domains (Figure 2), which is consistent with the binding mode observed in other syntenin-1/peptide complexes (Grembecka et al. 2006). The binding effects in the PDZ1+2 tandem are more pronounced for the PDZ2 domain, as also seen in the earlier NMR study of syntenin-1 interactions with syndecan, neurexin, and ephrin B-derived hexapeptides (Grembecka et al. 2006).

Given that PDZ domains recognize small linear motifs on cognate protein targets, the use of short peptides to mimic protein–PDZ interactions is a common experimental strategy to unravel relevant physiological interactions for fundamental research purposes (Manjunath et al. 2018), but it has its limitations. In particular, biophysical assays performed in dilute solutions of isolated syntenin-1 PDZ domains and short peptide ligands report very weak binding with K_D values in the millimolar range (Figure 2) (Grembecka et al. 2006; Latysheva et al. 2006), which is clearly insufficient to sustain a physiological interaction. We previously highlighted the importance of syntenin-1 as a potential recruiter of proteins into EVs (Lim et al. 2021). A compelling hypothesis is that blocking syntenin-1/viral protein interactions could elicit a two-pronged inhibitory activity: (i) at the viral budding step of enveloped virus replication where syntenin-1 could connect viral particles to the ESCRT pathway, and (ii) in cell-to-cell viral transmission and inflammatory immune response induction by exosomes containing syntenin-1/viral proteins complexes. In this work, we compared two previously described small molecules, an inhibitor of the syntenin-1-exosomal pathway disrupting tumour exosomal communication in breast carcinoma cells (Leblanc et al. 2020), and an inhibitor of Tax-1/hDLG-1 interaction impairing HTLV-1 transmission (Maseko et al. 2023), for their abilities to also inhibit the Tax-1/syntenin-1 interaction. Our results suggest that targeting the presence of viral or cellular oncogenes in EVs could affect their transport between cells and provide an alternative inhibition strategy.

A proteomic analysis of the EVs following treatment with a Tax-1/syntenin-1 interaction inhibitor shows that the proteins normally dysregulated during HTLV-1 infection were impacted (Figure 4A). For example, COL4A2, a component of the viral biofilm known to be induced by Tax-1 (Millen et al. 2019) and which, in turn, promotes viral transmission, was downregulated by the small molecule in EVs. Several other proteins that are upregulated in HTLV-1 infection, like the tetraspanins, were impacted by the same treatment. The reduction in levels of those proteins in EVs may explain as to why the EVs from treated cells do not promote cell-to-cell viral transmission compared to the control (Figure 3I). Interestingly, the inhibition of the syntenin-1/Tax-1 interaction was correlated with lower abundances of both proteins in EVs and concomitant limits of viral transmission. Lower expression of syntenin-1 in EVs can also be attributed to the presence of specific miRNAs, as previously reported (Lee et al. 2023). We found six experimentally-validated miRNAs known to bind to syntenin-1 differentially expressed in EVs of HTLV-1-infected cells treated with the iTax/PDZ-01 small molecule. Two of them, miR-629-5p and miR-944, exhibit opposite expression levels compared to syntenin-1 protein, suggesting two levels of inhibition of syntenin-1 in EVs from HTLV-1-infected cells treated with the iTax/PDZ-01 small molecule, and a possible synergy with miRNA targeting syntenin-1. In our study, treatment with iTax/PDZ-01 revealed both shared and divergent effects on EV cargo in infected (HuT 102) and non-infected (Jurkat) cells. Proteomic analysis showed approximately 37% overlap in DA proteins between the two cell types, although the magnitude of these changes was significantly greater in HuT 102 EVs, suggesting a heightened sensitivity of infected cells to the compound. Similarly, small RNA sequencing revealed a broader response in HuT 102 cells, with 280 DA miRNAs compared to only 86 in Jurkat, 70% of which were shared. These observations indicate that iTax/PDZ-01 modulates core vesicle pathways in both cell types, likely through its interaction with syntenin-1, but the presence of HTLV-1 significantly amplifies its regulatory effects. This differential response underscores the compound's potential selectivity in targeting virus-altered vesicle biogenesis and cargo sorting.

MiRNAs were discovered three decades ago (Nobel Prize to Victor Ambros, Gary Ruvkun in 2024) and are now well known as wide-range genetic regulators of cell division, proliferation and death. The miRNA database (http://mirbase.org/) contains about 50,000 entries across 217 organisms, including 1917 for human (Kozomara et al. 2019). They act by base-pairing to complementary mRNA targets, which affect their translation (Ambros 2003; Lee and Ambros 2001; Ambros 2024). Although aberrant expression of miRNAs is associated with various diseases, including cancer and viral infections, their applications in drug discovery remains limited, but should benefit from the current trend of enabled RNA therapeutics (Jones 2018; Teng et al. 2021). Particularly, the use of miRNA mimics and anti-microRNAs as potential antivirals is supported by numerous fundamental studies including in *Caenorhabditis elegans*, where small RNA and microRNA pathways modulate antiviral defence by regulating immunity and metabolism pathways (Seetharaman et al. 2024; Mao et al. 2022, 2020; Fischer et al. 2013). Unlike other RNA therapeutics such as mRNA vaccines or siRNA, mimics and anti-miRs suffer from their pleiotropic functional activities, and most of them fail at phase 2 in clinical trials. Examples include miR-34a (Mirna Therapeutics) or miR-29b (Viridian Therapeutics), as well as anti-miRs of miR-21 (Regulus

Therapeutics) or anti-miR-122, which were terminated in phase 1 or 2 due to their toxicity effects (What will it take to get miRNA therapies to market? 2024). To the best of our knowledge, as of 2024 there is still no miRNA mimics or anti-microRNAs used as antivirals in any clinical trial (https://clinicaltrials.gov/). Target specificity will be crucial to repurpose miRNA mimics and anti-miRs as innovative antivirals.

In this study, we show for the first time that there is an interplay between syntenin-1 mRNA expression and miR-320c, as seen in concentration dependent decrease in *SDCBP* mRNA expression in HTLV-1 cells treated with an miR-320c mimic (Figure 5D). This miR-320c mimic also had the highest change compared to the control (64-fold) in the EVs treated with an inhibitor of syntenin-1/Tax-1 interaction (Figure 5C). Again, cells treated with the miR-320c mimic caused a concentration dependent decrease in HTLV-1 *GAG* mRNA expression, and inhibition of cell-to-cell viral transmission (Figure 5E,F). In contrast, treatment of infected cells with a miR-320c inhibitor led to increased expression of syntenin-1 and GAG, thereby enhancing viral transmission (Figure 5G–J). We thus provide evidence that the miR-320 family could be associated with HTLV-1 infection. Interestingly, the miR-320c family has also been reported to be down regulated in some cancers and in patients with SARS-CoV-2-induced severe respiratory failures (Liang et al. 2021; Duecker et al. 2021). We conclude that a mimic of miR-320c could be used as an antiviral against HTLV-1 transmission. In addition to target selectivity/specificity, our study is also a proof-of-concept that EVs could be used as delivery tools for antiviral miRNAs, taking advantage of a natural infection route. Just as the identification of the main immunogenic proteins of a pathogenic virus allows rapid development of candidate vaccines, systematic PPI interactome mapping is of utmost importance to delineate druggable virus-host PPI targets. Therefore, combining viral-host PPI inhibitors and microRNA mimics (or anti-miRNAs) has the potential to drive future discovery of innovative antivirals.

Author Contributions

Conceptualization: Sibusiso B. Maseko., Jean-Claude Twizere and Alexander N. Volkov. **Methodology**: Sibusiso B. Maseko, Jedidja Puttemans, **Investigation**: Sibusiso B. Maseko, Inge Van Molle, Thandokuhle Ntombela, Karim Blibek, Julien Olivet, Manon Degey, Dominique Baiwir, Jedidja Puttemans, Julie Joseph, Jeremy Blavier, Deeya Saha, Malik Hamaidia, Alexander N. Volkov and Jean-Claude Twizere, Yasmine Brammerloo. **Formal analysis**: Sibusiso B. Maseko, Dae-Kyum Kim, Makon-Sébastien Njock, Jean-Claude Twizere, Inge Van Molle, Jedidja Puttemans and Alexander N. Volkov **Resources**: Franck Dequiedt, Steven Ballet, Alexander N. Volkov, Kourosh Salehi-Ashtiani and Jean-Claude Twizere. **Writing Original Draft**: Sibusiso B. Maseko, Karim Blibek, Inge Van Molle, Alexander N. Volkov and Jean-Claude Twizere. **Writing, Review and Editing**: Sibusiso B. Maseko, Pascale Zimmermann, Pooja Jain, Piel Geraldine, Franck Dequiedt, Alexander N. Volkov, Steven Ballet, Jean-Claude Twizere and Kourosh Salehi-Ashtiani. **Supervision**: Jean-Claude Twizere, Alexander N. Volkov, and Franck Dequiedt, Steven Ballet, **Funding Acquisition**: Franck Dequiedt, Alexander N. Volkov, Steven Ballet and Jean-Claude Twizere.

Acknowledgements

Computational resources have been provided by the Consortium des Équipements de Calcul Intensif (CÉCI), funded by the Fonds de la Recherche Scientifique (FRS-FNRS, Belgium) under Grant No. 2.5020.11 and by the Walloon Region. We thank the Genomics, Bioinformatics, Proteomics and Viral Vectors core facilities of the University of Liege for their services.

Conflicts of Interest

The authors declare no competing interests

Data Availability Statement

All data and materials used in the analyses are described in this manuscript. Plasmids and vectors are available via materials transfer agreements (MTAs)

References

Alais, S., H. Dutartre, and R. Mahieux. 2017. "Quantitative Analysis of Human T-Lymphotropic Virus Type 1 (HTLV-1) Infection Using Co-Culture With Jurkat LTR-Luciferase or Jurkat LTR-GFP Reporter Cells." *Methods in Molecular Biology* 1582: 47–55.

Al Sharif, S., D. O. Pinto, G. A. Mensah, et al. 2020. "Extracellular Vesicles in HTLV-1 Communication: The Story of an Invisible Messenger." *Viruses* 12, no. 12: 1422.

Amacher, J. F., L. Brooks, T. H. Hampton, and D. R. Madden. 2020. "Specificity in PDZ-Peptide Interaction Networks: Computational Analysis and Review." *Journal of Structural Biology X* 4: 100022.

Amaral, A. J., J. Andrade, R. B. Foxall, et al. 2017. "miRNA Profiling of Human Naive CD4 T Cells Links miR-34c-5p to Cell Activation and HIV Replication." *EMBO Journal* 36, no. 3: 346–360.

Ambros, V. 2003. "MicroRNA Pathways in Flies and Worms: Growth, Death, Fat, Stress, and Timing." *Cell* 113, no. 6: 673–676.

Ambros, V. 2024. "MicroRNA-Mediated Gene Regulation and the Resilience of Multicellular Animals." *Postepy Biochemii* 70, no. 1: 62–70.

Anderson, M. R., F. Kashanchi, and S. Jacobson. 2016. "Exosomes in Viral Disease." *Neurotherapeutics* 13, no. 3: 535–546.

Arone, C., S. Martial, J. Burlaud-Gaillard, et al. 2023. "HTLV-1 Biofilm Polarization Maintained by Tetraspanin CD82 Is Required for Efficient Viral Transmission." *mBio* 14, no. 6: e01326-23.

Baietti, M. F., Z. Zhang, E. Mortier, et al. 2012. "Syndecan–Syntenin–ALIX Regulates the Biogenesis of Exosomes." *Nature Cell Biology* 14, no. 7: 677–685.

Bangham, C. R. 2000. "HTLV-1 Infections." *Journal of Clinical Pathology* 53, no. 8: 581–586.

Bangham, C. R. M., A. Araujo, Y. Yamano, and G. P. Taylor. 2015. "HTLV-1-Associated Myelopathy/Tropical Spastic Paraparesis." *Nature Reviews Disease Primers* 1: 15012.

Barnard, A. L., T. Igakura, Y. Tanaka, G. P. Taylor, and C. R. M. Bangham. 2005. "Engagement of Specific T-Cell Surface Molecules Regulates Cytoskeletal Polarization in HTLV-1-Infected Lymphocytes." *Blood* 106, no. 3: 988–995.

Baryshnikova, A. 2016. "Systematic Functional Annotation and Visualization of Biological Networks." *Cell Systems* 2, no. 6: 412–421.

Bazarbachi, A. 2016. "Tax Fingerprint in Adult T-Cell Leukemia." *Blood* 127, no. 14: 1737–1738.

Boxus, M., J.-C. Twizere, S. Legros, J.-F. Dewulf, R. Kettmann, and L. Willems. 2008. "The HTLV-1 Tax Interactome." *Retrovirology* 5: 76.

Caillet-Saguy, C., F. Durbesson, V. V. Rezelj, et al. 2021. "Host PDZ-Containing Proteins Targeted by SARS-CoV-2." *FEBS Journal* 288, no. 17: 5148–5162.

Caillet-Saguy, C., and N. Wolff. 2021. "PDZ-Containing Proteins Targeted by the ACE2 Receptor." *Viruses* 13, no. 11: 2281.

Capone, E., S. Iacobelli, and G. Sala. 2021. "Role of Galectin 3 Binding Protein in Cancer Progression: A Potential Novel Therapeutic Target." *Journal of Translational Medicine* 19, no. 1: 405.

Cassonnet, P., C. Rolloy, G. Neveu, et al. 2011. "Benchmarking a Luciferase Complementation Assay for Detecting Protein Complexes." *Nature Methods* 8, no. 12: 990–992.

Castro-Cruz, M., L. Hyka, G. Daaboul, et al. 2023. "PDZ Scaffolds Regulate Extracellular Vesicle Production, Composition, and Uptake." *Proceedings of the National Academy of Sciences* 120, no. 38: e2310914120.

Cierpicki, T., J. H. Bushweller, and Z. S. Derewenda. 2005. "Probing the Supramodular Architecture of a Multidomain Protein: The Structure of Syntenin in Solution." *Structure (London, England)* 13, no. 2: 319–327.

Cook, L., A. Melamed, H. Yaguchi, and C. R. M. Bangham. 2017. "The Impact of HTLV-1 on the Cellular Genome." *Current Opinion in Virology* 26: 125–131.

Cox, J., and M. Mann. 2008. "MaxQuant Enables High Peptide Identification Rates, Individualized p.p.b.-Range Mass Accuracies and Proteome-Wide Protein Quantification." *Nature Biotechnology* 26, no. 12: 1367–1372.

Currer, R., R. Van Duyne, E. Jaworski, et al. 2012. "HTLV Tax: A Fascinating Multifunctional Co-Regulator of Viral and Cellular Pathways." *Frontiers in Microbiology* 3: 406.

Delaglio, F., S. Grzesiek, G. Vuister, G. Zhu, J. Pfeifer, and A. D. Bax. 1995. "NMRPipe: A Multidimensional Spectral Processing System Based on UNIX Pipes." *Journal of Biomolecular NMR* 6, no. 3: 277–293.

Du, X., Y. Yang, G. Xiao, et al. 2020. "Respiratory Syncytial Virus Infection-Induced Mucus Secretion by Down-Regulation of miR-34b/c-5p Expression in Airway Epithelial Cells." *Journal of Cellular and Molecular Medicine* 24, no. 21: 12694–12705.

Duecker, R. P., E. H. Adam, S. Wirtz, et al. 2021. "The MiR-320 Family Is Strongly Downregulated in Patients With COVID-19 Induced Severe Respiratory Failure." *International Journal of Molecular Sciences* 22, no. 19: 10351.

Fakhar, A. Z., J. Liu, and K. M. Pajerowska-Mukhtar. 2023. "Dynamic Enrichment for Evaluation of Protein Networks (DEEPN): a High Throughput Yeast Two-Hybrid (Y2H) Protocol to Evaluate Networks." *Methods in Molecular Biology* 2690: 179–192.

Fawzy, M. P., H. A. F. M. Hassan, N. K. Sedky, M. S. Nafie, R. A. Youness, and S. A. Fahmy. 2024. "Revolutionizing Cancer Therapy: Nanoformulation of miRNA-34 – Enhancing Delivery and Efficacy for Various Cancer Immunotherapies: A Review." *Nanoscale Advances* 6, no. 21: 5220–5257.

Fischer, S. E., Q. Pan, P. C. Breen, et al. 2013. "Multiple Small RNA Pathways Regulate the Silencing of Repeated and Foreign Genes in *C. elegans*." *Genes & Development* 27, no. 24: 2678–2695.

Fujikawa, D., S. Nakagawa, M. Hori, et al. 2016. "Polycomb-Dependent Epigenetic Landscape in Adult T-Cell Leukemia." *Blood* 127, no. 14: 1790–1802.

Galloway, N. L. K., G. Doitsh, K. M. Monroe, et al. 2015. "Cell-to-Cell Transmission of HIV-1 Is Required to Trigger Pyroptotic Death of Lymphoid-Tissue-Derived CD4 T Cells." *Cell Reports* 12, no. 10: 1555–1563.

Grembecka, J., T. Cierpicki, Y. Devedjiev, et al. 2006. "The Binding of the PDZ Tandem of Syntenin to Target Proteins." *Biochemistry* 45, no. 11: 3674–3683.

He, B., A. Sridhar, M. Thiry, O. Haenen, A. F. C. Vanderplasschen, and O. Donohoe. 2025. "Genomic and Phenotypic Characterization of a Novel Virulent Strain of Cyvirus Cyprinidallo 2 Originating From an Outbreak in the Netherlands." *Viruses* 17, no. 5: 658.

Human, T. 2008. "Highly Enhanced Expression of CD70 On." *Journal of Virology* 82, no. 8: 3843.

Igakura, T., J. C. Stinchcombe, P. K. C. Goon, et al. 2003. "Spread of HTLV-I Between Lymphocytes by Virus-Induced Polarization of the Cytoskeleton." *Science* 299, no. 5613: 1713–1716.

Imjeti, N. S., K. Menck, A. L. Egea-Jimenez, et al. 2017. "Syntenin Mediates SRC Function in Exosomal Cell-to-Cell Communication." *PNAS* 114, no. 47: 12495–12500.

Ivarsson, Y., R. Arnold, M. Mclaughlin, et al. 2014. "Large-Scale Interaction Profiling of PDZ Domains Through Proteomic Peptide-Phage Display Using Human and Viral Phage Peptidomes." *PNAS* 111, no. 7: 2542–2547.

Jaworski, E., A. Narayanan, R. Van Duyne, et al. 2014. "Human T-Lymphotropic Virus Type 1-Infected Cells Secrete Exosomes That Contain Tax Protein." *Journal of Biological Chemistry* 289, no. 32: 22284–22305.

Jimenez-Guardeño, J. M., J. L. Nieto-Torres, M. L. Dediego, et al. 2014. "The PDZ-Binding Motif of Severe Acute respiratory Syndrome Coronavirus Envelope Protein Is a Determinant of Viral Pathogenesis." *PLOS Pathogens* 10, no. 8: e1004320.

Jones, D. 2018. "Setbacks Shadow microRNA Therapies in the Clinic." *Nature Biotechnology* 36, no. 10: 909–910.

Jørgensen, K., M. Skrede, V. Cruciani, S. - O. Mikalsen, A. Slipicevic, and V. A. Flørenes. 2005. "Phorbol ester phorbol-12-myristate-13-acetate promotes anchorage-independent growth and survival of melanomas through MEK-independent activation of ERK1/2." *Biochemical and Biophysical Research Communications* 329, no. 1: 266–274. https://doi.org/10.1016/j.bbrc.2005.01.143.

Kannt, A., S. Young, and D. S. Bendall. 1996. "The Role of Acidic Residues of Plastocyanin in Its Interaction With Cytochrome *f*." *Biochimica et Biophysica Acta (BBA)—Bioenergetics* 1277, no. 1: 115–126.

Kashyap, R., M. Balzano, B. Lechat, et al. 2021. "Syntenin-Knock Out Reduces Exosome Turnover and Viral Transduction." *Scientific Reports* 11, no. 1: 4083.

Kfoury, Y., R. Nasr, C. Journo, R. Mahieux, C. Pique, and A. Bazarbachi. 2012. "The Multifaceted Oncoprotein Tax: Subcellular Localization, Post-translational Modifications, and NF-κB Activation." *Advances in Cancer Research* 113: 85–120.

Kim, D.-K., J. Lee, S. R. Kim, et al. 2015. "EVpedia: A Community Web Portal for Extracellular Vesicles Research." *Bioinformatics* 31, no. 6: 933–939.

Kim, Y., G. A. Mensah, S. Al Sharif, et al. 2021. "Extracellular Vesicles From Infected Cells Are Released Prior to Virion Release." *Cells* 10, no. 4: 781.

Kimata, J. T., F.-H. Wong, J. J. Wang, and L. Ratner. 1994. "Construction and Characterization of Infectious Human T-Cell Leukemia Virus Type 1 Molecular Clones." *Virology* 204, no. 2: 656–664.

Kowal, J., M. Tkach, and C. Théry. 2014. "Biogenesis and Secretion of Exosomes." *Current Opinion in Cell Biology* 29: 116–125.

Kozomara, A., M. Birgaoanu, and S. Griffiths-Jones. 2019. "miRBase: From microRNA Sequences to Function." *Nucleic Acids Research* 47, no. D1: D155–D162.

Kwok, R. P. S., M. E. Laurance, J. R. Lundblad, et al. 1996. "Control of cAMP-Regulated Enhancers by the Viral Transactivator Tax Through CREB and the Co-Activator CBP." *Nature* 380, no. 6575: 642–646.

Lambourne, L., A. Yadav, Y. Wang, et al. 2021. "Binary Interactome Models of Inner-Versus Outer-Complexome Organisation." *BioRxiv* 03.16.435663.

Latysheva, N., G. Muratov, S. Rajesh, et al. 2006. "Syntenin-1 Is a New Component of Tetraspanin-Enriched Microdomains: Mechanisms and Consequences of the Interaction of Syntenin-1 With CD63." *Molecular and Cellular Biology* 26, no. 20: 7707–7718.

Leblanc, R., R. Kashyap, K. Barral, et al. 2020. "Pharmacological Inhibition of Syntenin PDZ2 Domain Impairs Breast Cancer Cell Activities and Exosome Loading With Syndecan and EpCAM Cargo." *Journal of Extracellular Vesicles* 10, no. 2: e12039.

Lee, K.-M., E.-C. Seo, J.-H. Lee, H.-J. Kim, and C. Hwangbo. 2023. "The Multifunctional Protein Syntenin-1: Regulator of Exosome Biogenesis,

Cellular Function, and Tumor Progression." *International Journal of Molecular Sciences* 24, no. 11: 9418.

Lee, R. C., and V. Ambros. 2001. "An Extensive Class of Small RNAs in *Caenorhabditis elegans*." *Science* 294, no. 5543: 862–864.

Liang, Y., S. Li, and L. Tang. 2021. "MicroRNA 320, an Anti-Oncogene Target miRNA for Cancer Therapy." *Biomedicines* 9, no. 6: 591.

Lim, H. J., H. Yoon, H. Kim, et al. 2021. "Extracellular Vesicle Proteomes Shed Light on the Evolutionary, Interactive, and Functional Divergence of Their Biogenesis Mechanisms." *Frontiers in Cell and Developmental Biology* 9: 734950.

Luck, K., D.-K. Kim, L. Lambourne, et al. 2020. "A Reference Map of the Human Binary Protein Interactome." *Nature* 580, no. 7803: 402–408.

Machado, C. B., L. S. Da Cunha, J. H. Da. S. Maués, et al. 2022. "Role of miRNAs in Human T Cell Leukemia Virus Type 1 Induced T Cell Leukemia: A Literature Review and Bioinformatics Approach." *International Journal of Molecular Sciences* 23, no. 10: 5486.

Manjunath, G. P., P. L. Ramanujam, and S. Galande. 2018. "Structure Function Relations in PDZ-Domain-Containing Proteins: Implications for Protein Networks in Cellular Signalling." *Journal of Biosciences* 43, no. 1: 155–171.

Mao, K., P. Breen, and G. Ruvkun. 2020. "Mitochondrial Dysfunction Induces RNA Interference in *C. elegans* Through a Pathway Homologous to the Mammalian RIG-I Antiviral Response." *PLOS Biology* 18, no. 12: e3000996.

Mao, K., P. Breen, and G. Ruvkun. 2022. "The *Caenorhabditis elegans* ARIP-4 DNA Helicase Couples Mitochondrial Surveillance to Immune, Detoxification, and Antiviral Pathways." *PNAS* 119, no. 49: e2215966119.

Maseko, S. B., Y. Brammerloo, I. Van Molle, et al. 2023. "Identification of Small Molecule Antivirals Against HTLV-1 by Targeting the hDLG1-Tax-1 Protein-protein Interaction." *Antiviral Research* 217: 105675.

Matsuoka, M., and K. T. Jeang. 2011. "Human T-Cell Leukemia Virus Type 1 (HTLV-1) and Leukemic Transformation: Viral Infectivity, Tax, HBZ and Therapy." *Oncogene* 30, no. 12: 1379–1389.

Mazurov, D., G. Heidecker, and D. Derse. 2007. "The Inner Loop of Tetraspanins CD82 and CD81 Mediates Interactions With Human T Cell Lymphotrophic Virus Type 1 Gag Protein." *Journal of Biological Chemistry* 282, no. 6: 3896–3903.

Millen, S., C. Gross, N. Donhauser, M. C. Mann, J. M. Péloponèse Jr., and A. K. Thoma-Kress. 2019. "Collagen IV (COL4A1, COL4A2), a Component of the Viral Biofilm, Is Induced by the HTLV-1 Oncoprotein Tax and Impacts Virus Transmission." *Frontiers in Microbiology* 10: 2439.

Muller, M., P. Cassonnet, M. Favre, Y. Jacob, and C. Demeret. 2013. "A Comparative Approach to Characterize the Landscape of Host-Pathogen Protein-Protein Interactions." *Journal of Visualized Experiments: JoVE* no. 77: e50404.

Nardella, C., L. Visconti, F. Malagrinò, et al. 2021. "Targeting PDZ Domains as Potential Treatment for Viral Infections, Neurodegeneration and Cancer." *Biology Direct* 16, no. 1: 15.

Nejmeddine, M., and C. R. M. Bangham. 2010. "The HTLV-1 Virological Synapse." *Viruses* 2, no. 7: 1427–1447.

Nejmeddine, M., V. S. Negi, S. Mukherjee, et al. 2009. "HTLV-1-Tax and ICAM-1 Act on T-Cell Signal Pathways to Polarize the Microtubule-Organizing Center at the Virological Synapse." *Blood* 114, no. 5: 1016–1025.

Neveu, G., P. Cassonnet, P.-O. Vidalain, et al. 2012. "Comparative Analysis of Virus-Host Interactomes With a Mammalian High-Throughput Protein Complementation Assay Based on Gaussia princeps Luciferase." *Methods (San Diego, Calif.)* 58, no. 4: 349–359.

Nozuma, S., R. Kubota, and S. Jacobson. 2020. "Human T-Lymphotropic Virus Type 1 (HTLV-1) and Cellular Immune Response in HTLV-1-Associated Myelopathy/Tropical Spastic Paraparesis." *Journal of Neurovirology* 26, no. 5: 652–663.

Parikh, J. R., B. Klinger, Y. Xia, J. A. Marto, and N. Blüthgen. 2010. "Discovering Causal Signaling Pathways Through Gene-expression Patterns." *Nucleic Acids Research* 38, no. suppl_ 2: W109–W117.

Pérès, E., J. Blin, E. P. Ricci, et al. 2018. "PDZ Domain-Binding Motif of Tax Sustains T-Cell Proliferation in HTLV-1-Infected Humanized Mice." *PLOS Pathogens* 14, no. 3: e1006933.

Pinto, D. O., C. Demarino, M. L. Pleet, et al. 2019. "HTLV-1 Extracellular Vesicles Promote Cell-to-Cell Contact." *Frontiers in Microbiology* 10: 2147.

Pokhrel, N. K., A. R. Panfil, H. Habib, et al. 2024. "HTLV-1 Infected T Cells Cause Bone Loss via Small Extracellular Vesicles." *Journal of Extracellular Vesicles* 13, no. 10: e12516.

Santoni, M.-J., R. Kashyap, L. Camoin, and J.-P. Borg. 2020. "The Scribble family in Cancer: Twentieth Anniversary." *Oncogene* 39, no. 47: 7019–7033.

Seetharaman, A., H. Galagali, E. Linarte, et al. 2024. "*Caenorhabditis elegans* SynMuv B Gene Activity Is Down-Regulated During a Viral Infection to Enhance RNA Interference." *BioRxiv* .

Seiki, M., J. Inoue, M. Hidaka, and M. Yoshida. 1988. "Two Cis-Acting Elements Responsible for Posttranscriptional Trans-Regulation of Gene Expression of Human T-Cell Leukemia Virus Type I." *PNAS* 85, no. 19: 7124–7128.

Sieburg, M., A. Tripp, J.-W. Ma, and G. Feuer. 2004. "Human T-Cell Leukemia Virus Type 1 (HTLV-1) and HTLV-2 Tax Oncoproteins Modulate Cell Cycle Progression and Apoptosis." *Journal of Virology* 78, no. 19: 10399–10409.

Simonis, N., J.-F. Rual, I. Lemmens, et al. 2012. "Host-Pathogen Interactome Mapping for HTLV-1 and -2 Retroviruses." *Retrovirology* 9, no. 1: 26.

Sommerova, L., M. Anton, P. Bouchalova, et al. 2019. "The Role of miR-409-3p in Regulation of HPV16/18-E6 mRNA in Human Cervical High-Grade Squamous Intraepithelial Lesions." *Antiviral Research* 163: 185–192.

Teng, M., Z. J. Xia, N. Lo, K. Daud, and H. H. He. 2021. "Assembling the RNA Therapeutics Toolbox." *Medicinal Reviews* 4, no. 2: 110–128.

Théry, C., K. W. Witwer, E. Aikawa, et al. 2018. "Minimal Information for Studies of Extracellular Vesicles 2018 (MISEV2018): A Position Statement of the International Society for Extracellular Vesicles and Update of the MISEV2014 Guidelines." *Journal of Extracellular Vesicles* 7, no. 1: 1535750.

Tyanova, S., T. Temu, P. Sinitcyn, et al. 2016. "The Perseus Computational Platform for Comprehensive Analysis of (prote) Omics Data." *Nature Methods* 13, no. 9: 731–740.

Van Criekinge, W., and R. Beyaert. 1999. "Yeast Two-Hybrid: State of the Art." *Biological Procedures Online* 2: 1–38.

Vandermeulen, C., T. O'Grady, J. Wayet, et al. 2021. "The HTLV-1 Viral Oncoproteins Tax and HBZ Reprogram the Cellular mRNA Splicing Landscape." *Plos Pathogens* 17, no. 9: e1009919.

Van Niel, G., G. d'Angelo, and G. Raposo. 2018. "Shedding Light on the Cell Biology of Extracellular Vesicles." *Nature Reviews Molecular Cell Biology* 19, no. 4: 213–228.

Volkov, A. N., and N. A. van Nuland. 2013. "Solution NMR Study of the Yeast Cytochrome c Peroxidase: Cytochrome c Interaction." *Journal of Biomolecular NMR* 56, no. 3: 255–263.

Vranken, W. F., W. Boucher, T. J. Stevens, et al. 2005. "The CCPN Data Model for NMR Spectroscopy: Development of a Software Pipeline." *Proteins* 59, no. 4: 687–696.

2024. "What Will It Take to Get miRNA Therapies to Market?." *Nature Biotechnology* 42, no. 11: 1623–1624.

Xie, L., B. Yamamoto, A. Haoudi, O. J. Semmes, and P. L. Green. 2006. "PDZ Binding Motif of HTLV-1 Tax Promotes Virus-Mediated T-Cell Proliferation In Vitro and Persistence In Vivo." *Blood* 107, no. 5: 1980–1988.

Zhang, Y., Y. Liu, H. Liu, and W. H. Tang. 2019. "Exosomes: Biogenesis, Biologic Function and Clinical Potential." *Cell & Bioscience* 9, no. 1: 19.

Zhao, L. J., and C. Z. Giam. 1991. "Interaction of the Human T-Cell Lymphotrophic Virus Type I (HTLV-I) Transcriptional Activator Tax With Cellular Factors That Bind Specifically to the 21-Base-Pair Repeats in the HTLV-I Enhancer." *PNAS* 88, no. 24: 11445–11449.

Supporting Information

Additional supporting information can be found online in the Supporting Information section.

Supporting Table 1: jev270137-sup-0001-TableS1.xlsx **Supporting Table 2**: jev270137-sup-0002-TableS2.xlsx **Supporting Table 3**: jev270137-sup-0003-TableS3.xlsx **Supporting Table 4**: jev270137-sup-0004-TableS4.xlsx **Supporting Table 5**: jev270137-sup-0005-TableS5.xlsx Supplementary Data are available online **Supporting Fig.1: A comprehensive analysis of the Tax-1 interactome with human PDZ-containing proteins. A,** PPIs between Tax-1 and human PDZ domain-containing proteins identified by yeast 2-hybrid (Y2H) and validated by GPCA or using a pull-down assay (blue); and known PPIs from the literature (yellow). **B,** Literature reported interactions between Tax-1 and human PDZ domain-containing proteins. **C**, Heat maps of the Y2H assay by testing a library of 244 individualized PDZ domain-containing proteins fused to AD against DB-Tax-1. A growth score of '0', '1' or '2' indicates a null, weak or strong interaction, respectively. **D**, Representative Y2H assay plate lacking tryptophan (Trp), leucine (Leu), and histidine (His) where a growth score of '0', '1' or '2' indicates a null, weak or strong interaction between DB-Tax-1 and PDZ-domain containing proteins fused to AD, respectively. **E**, Representative GST-pull-down analyses of proteins encoded by Flag-fused open reading frames (ORFs) available in the human ORFeome collection. **Supporting Fig.2: Tax-1 PDZ interactome with the cytoskeleton and control syntenin-1 NMR-experiments with Tax-1 PBM 4mer and 6mer-N peptides**. GO analysis was done using the 58 Tax1/PDZ interactors and the cytoskeleton was significantly enriched. The visualization shows the Tax-1 PDZ interactors found in the cytoskeleton and their binding partners are shown. SDCBP has the most interactions among the 14 PDZ involved in the cytoskeleton. Visualization was done using cytoscape. **B** $\Delta\delta$avg of 15N syntenin-1 PDZ1+2 tandem in the presence of 6 molar equivalents of PBM 4mer. Residues with backbone amides broadened beyond the detection limit upon complex formation are indicated by red bars. **C**, Chemical shift mapping of the PBM 4mer binding. The molecular surface of syntenin-1 PDZ1+2 tandem is colored as in Figure 2B. The modeled PBM peptides, bound to the canonical PDZ sites, are shown in sticks. **D**, $\Delta\delta$avg of the 15N syntenin-1 PDZ1+2 tandem in the presence of 7 molar equivalents of 6mer-N. Several residues with significant binding shifts are labelled. Interaction between syntenin with Tax-1 and syntenin with Tax-2 in FP **Supporting Fig.3: Inhibition of viral transmission, characterization of jurkat and HuT 102 EVs**. A, schematic representation of the co-culture experiment. **B**, Inhibition of HTLV-1 cell to cell transmission by **syntOFF**. **C,** Inhibition of HTLV-1 cell to cell transmission by **iTax/PDZ-01**.D,**E**, NTA analysis of EVs from DMSO and iTax/PDZ-01 treated Jurkat cell lines. **F**, **G,** Representative TEM scale bar on images of EVs released from DMSO and iTax/PDZ-01 Jurkat cells showing the presence of EVs around 200 nm in diameter: scale bar = 200 nm. Western blot analysis of EVS Jurkat and HuT 102 cells following inactivation and removal contaminating virus particles prior to exosome extraction. The data points in the bar graphs represent the mean (n = 3); the errors are standard deviations from the mean. Statistical significance in was determined with a one-way ANOVA (*$p < 0.05$, **$p < 0.01$, ***$p < 0.001$, and ****$p < 0.0001$) in GraphPad Prism. **Supporting Fig.4: Comparative proteomics of EVs from Jurkat and HUT 102 cells**. Principal Component Analysis (PCA) of LFQ proteomics data from (**A**) Jurkat and (**B**) HuT 102 EVs. Samples cluster clearly by condition, demonstrating high reproducibility among biological replicates and distinct separation between groups. **(C)** Comparison of DE proteins from Jurkat and HUT 102 EVs. **(E)** Principal component analysis (PCA) of biological replicates**. (D**) Volcano plot showing 476 differentially abundant proteins in Jurkat EVs (green: downregulated; red: upregulated). **(E)** SPEED2 pathway analysis: x-axis shows z-scores (–1 to 1), bar heights indicate mean rank, and colors reflect adjusted *p* values. Barcode plot indicates query gene positions. Bates test used for significance. **(F)** Protein–protein interaction analysis of upregulated proteins using MCODE and Metascape; node size indicates degree from HuT 102 EVs **Supporting Fig.5: Analysis of miRNA Gene targets obtained from IPA, the effect of miR-320c in viral transmission and effect of miR-320d and e in infected cells and analysis of miRNA from Jurkat EVs. A**, Gene ontology analysis of the 14 gene targets from mass spectrometry data with opposite expression to their miRNA binders obtained in IPA (BP = Biological process, CC = Cellular Component, MF = molecular Function). **B**, miRNAs found in the set that have already been to bind to SDCBP (syntenin-1). **C**, Inhibition of cell to cell viral transmission following treatment with miR-320c mimic using C91 and Jurkat-LTR-Luc cells. C91 cells were first transfected with increasing miRNA concentration, the cells were then used the co-culture experiment. **D, E, F, G** The effect of miR320d and 320e in *SDCBP* and *GAG*, respectively. **H**, Quantification of miR-320c in iTax/PDZ-01 treated HuT 102 cells using RT-qPCR. **I**, Quantification of GAG mRNA expression in HUT102 cells following treatment with small molecule using RT-qPCR. J, Volcano plot showing all the miRNA determined, downregulated miRNAs are shown in green, up regulated are shown in red, and those not significantly affected are shown in black in Jurkat cells.,K, Comparason between DA miRNAs from Jurkat and HuT 102 EVs. The data points in the bar graphs represent the mean (n = 3); the errors are standard deviations from the mean. Statistical significance was determined with a one-way ANOVA (*$p < 0.05$, **$p < 0.01$, ***$p < 0.001$, and ****$p < 0.0001$) in GraphPad Prism.